Evaluating the EPICC-Model for Regional Air Quality Simulation: A Comparative Study with CAMx and CMAQ

Mengjie Lou[1], Qizhong Wu[1], Wending Wang[2,3,4], Huansheng Chen[2,3,4], Kai Cao[2], Xiaohan Fan[5], Dingyue Liang[5], FenFen Yu[5], Jiating Zhang[1], Wei Wang[6], Zifa Wang[2,3,4]

[1]Institute of Earth System Science, Faculty of Geographical Science, Beijing Normal University, Beijing, 100875, China
[2]State Key Laboratory of Atmospheric Environment and Extreme Meteorology, Institute of Atmospheric Physics, Chinese Academy of Sciences, Beijing, 100029, China
[3]State Key Laboratory of Atmospheric Boundary Layer Physics and Atmospheric Chemistry, Institute of Atmospheric Physics, Chinese Academy of Sciences, Beijing, 100029, China
[4]University of Chinese Academy of Sciences, Beijing, 100049, China
[5]3Clear Technology Co., Ltd., Beijing, 100029, China
[6]China National Environmental Monitoring Centre, Beijing, 100012, China

Correspondence: Qizhong Wu (wqizhong@bnu.edu.cn) and Wending Wang (wangwending@mail.iap.ac.cn)

Abstract

This study presents a systematic evaluation of the EPICC-Model developed in China for regional $PM_{2.5}$ and MDA8 O_3 simulations against established international models, using WRF meteorological fields and a multi-source integrated emission inventory. Results highlight the strengths of the EPICC-Model in several aspects: it achieves relatively high spatial consistency with measurements for $PM_{2.5}$, with an annual index of agreement (IOA) of 0.80, and accurately captures pollution patterns in heavily polluted North China. It also demonstrates improved performance in simulating summer O_3 peaks, reducing maximum bias by more than 20 μg m^{-3}; this performance may be partly associated with its inclusion of heterogeneous HONO formation and particulate nitrate photolysis. The model exhibits the highest hit rate (45.6%) for MDA8 O_3 pollution events exceeding 160 μg m^{-3} and successfully reproduces persistent pollution episodes. However, all models share common limitations, including insufficient capability in reproducing heavy pollution episodes, systematic underestimation of SO_4^{2-}, and uncertainties in SOA-related OC simulations. Future improvements should focus on refining secondary aerosol chemistry and emission inventories and further evaluating the representation of vertical turbulent mixing under stable boundary-layer conditions. This study benchmarks the performance of the EPICC-Model against established CTMs and identifies priorities for its further development and regional application.

1 Introduction

With rapid urbanization and industrialization, China faces increasingly severe multi-pollutant air quality challenges. Among them, fine particulate matter ($PM_{2.5}$) and ozone (O_3) are key threats to public health and ecosystems, and their coordinated control has become a priority. Specifically, $PM_{2.5}$ comprises both directly emitted particles and secondary components formed from SO_2, NOx, NH_3, and VOCs, with its levels also affected by regional transport and meteorology (Zhang et al., 2012; Jing et al., 2020; Zhai et al., 2021; Bao et al., 2023). Emission control policies have reduced population-weighted $PM_{2.5}$ exposure by ~48% from 2013 to 2020 (Xiao et al., 2022), yet severe winter haze episodes persist in regions like Beijing-Tianjin-Hebei. In contrast, O_3 is formed through photochemical reactions involving NO_x and VOCs, and its production exhibits nonlinear responses to precursor levels, characterized by NO_x-sensitive and VOC-sensitive regimes (Haagen-Smit and Fox, 1956; Sillman, 1999). Ambient O_3 levels are also strongly influenced by meteorological factors, including solar radiation, temperature, humidity, and boundary-layer dynamics (Li et al., 2019b; Gao et al., 2022). In many Chinese urban clusters, $PM_{2.5}$ concentrations have decreased, whereas warm-season maximum daily 8 h average (MDA8) O_3 concentrations increased at a rate of 1.2 ±1.3 ppb yr^{-1} during 2013-2022 (Wang et al., 2024).The combined pollution of $PM_{2.5}$ and O_3 exhibits complex spatiotemporal evolution patterns and formation mechanisms (Lyu et al., 2025; Zhu et al., 2023), posing significant challenges for sustained air quality improvement in China.

To better understand the formation of complex air pollution and assess control strategies, Chemical Transport Models (CTMs) are widely used for regional air quality analysis and policy evaluation (Li et al., 2021; Gao and Zhou, 2024). Representative CTMs include the Community Multiscale Air Quality Modeling System (CMAQ) developed by the U.S. Environmental Protection Agency (EPA) (Byun and Schere, 2006; Foley et al., 2010; Appel et al., 2017, 2021), the Comprehensive Air Quality Model with Extensions (CAMx) developed by Ramboll (Ramboll, 2024), WRF-Chem for regional-scale simulations (Grell et al., 2005), and GEOS-Chem, which is widely applied for global-scale studies (Eastham et al., 2018; The International GEOS-Chem User Community, 2025). However, current CTMs still exhibit significant uncertainties in simulating $PM_{2.5}$ and O_3 under specific pollution scenarios in China, primarily manifested as systematic biases in peak concentrations, spatiotemporal distribution errors, and inaccuracies in capturing seasonal variability (Bessagnet et al., 2016; Chen et al., 2019). Against this backdrop, China has developed the Emission and atmospheric Processes Integrated and Coupled Community Model (EPICC-Model) to enhance capabilities in simulating complex pollution processes. Supported by the National Natural Science Foundation of China (Major Program) and the Earth System Numerical Simulation Facility (EarthLab), the model was officially released on November 8, 2024 (EPICC-Model Working Group, 2026) (for detailed description, see Section 2.1).

As a newly released CTM, the EPICC-Model has undergone preliminary single-model performance evaluations (EPICC-Model Working Group, 2026; Wang et al., 2025), but systematic multi-model comparisons under nationwide, multi-season conditions remain lacking. Multi-model intercomparison not only helps reveal differences among models in pollutant transport, chemical reactions, and meteorological feedbacks, but also serves as a key approach to quantifying simulation uncertainties and improving model robustness and reliability (Carmichael et al., 2008). Although substantial efforts have been made in evaluating CTMs over China and East Asia, such as the MICS-Asia phase studies on $PM_{2.5}$ and O_3 (Chen et al., 2019; Gong

and Liao, 2019; Itahashi et al., 2020; Li et al., 2019a), regional comparisons in the Pearl River Delta (Wu et al., 2012), and recent multi-model analyses over eastern China (Gao et al., 2024), most focus on earlier-generation or established models. Likewise, large-scale assessments within CMIP5/6 have consistently revealed systematic biases in simulating $PM_{2.5}$ and components across China (Li et al., 2020; Ren et al., 2024). Given the structural innovations and representations in the EPICC-Model, it is both timely and necessary to conduct a systematic comparison with established CTMs over China, in order to comprehensively assess its strengths and weaknesses and provide a scientific basis for subsequent model improvement and application.

Therefore, this study implements a consistent model intercomparison framework to systematically compare the simulation performance of three models (EPICC-Model, CMAQ, and CAMx) for $PM_{2.5}$ and O_3 concentrations over China in 2021, based on a unified meteorological driving field and a multi-source integrated emission inventory. The objectives are to comprehensively assess the capabilities of the EPICC-Model, identify common issues and their potential causes across multiple models, and propose targeted improvements. The paper is structured as follows: Section 2 introduces the configuration schemes of the three models, emission data sources, the WRF-based meteorological forcing, and the evaluation of meteorological simulations. Section 3 presents the research results, including comparative analyses of the spatiotemporal distribution simulations of $PM_{2.5}$ and O_3, $PM_{2.5}$ chemical composition analysis, assessments of the Air Quality Index (AQI) and pollution forecast accuracy, as well as comparisons of model performance in simulating persistent pollution events. Section 4 summarizes the key findings and discusses future directions for model improvements and prospects.

2 Data and methods

2.1 Overview of simulation domain, period, and CTM configurations

This study employs a two-level nested grid configuration with the model domain centered at (35°N, 105°E). The outer domain covers East Asia with a 45 km horizontal resolution (228 × 165 grid cells), while the inner domain focuses on China at a 15 km resolution (465 × 300 grid cells), starting from grid point (36, 39) within the outer domain. All analyses and results are derived from the inner domain simulations. The simulation period extends from 12:00 UTC on 14 December 2020 to 18:00 UTC on 31 December 2021, with the initial 17.25 days (until 18:00 UTC on 31 December 2020) dedicated to model spin-up.

To systematically evaluate the operational model configurations, this study employs consistent meteorological driving fields generated by the Weather Research and Forecasting (WRF) model and a harmonized multi-source emission inventory to drive year-long simulations using the EPICC-Model, CAMx, and CMAQ. The EPICC-Model is a three-dimensional tropospheric CTM developed in China with an independent modular framework (EPICC-Model Working Group, 2026). Several major process-level routines and numerical algorithms were inherited or adapted from CAMx and CMAQ, whose foundational contributions are explicitly acknowledged. Building on these foundations, the EPICC development team designed a modular and plug-in architecture and independently integrated several specialized chemistry treatments, including sulfate formation, heterogeneous HONO production, and N_2O_5 hydrolysis.

Featuring highly modular architecture and parallel computing capabilities, it simulates key physical and chemical processes including emissions, transport, gas-phase and heterogeneous reactions, aerosol thermodynamics, and dry/wet deposition. CAMx (Ramboll, 2020) is a versatile photochemical grid model widely used for air quality scientific assessments and policy support. It follows the "one atmosphere" approach, accommodating pollution simulations from urban to regional scales (Emery et al., 2024). CMAQ (EPA, 2021) is a continuously evolving open-source modeling platform featuring an open architecture and multi-processor parallel computing capabilities. It efficiently simulates air pollution processes including O_3, particulate matter, toxic pollutants, and acid deposition (US EPA, 2021).

Table 1. Key configuration schemes of the EPICC-Model, CMAQ, and CAMx.

	EPICC-Model	CAMx	CMAQ
Model version	v1.0	v7.0	v5.3.3
Vertical layers	$20\sigma_z$ layers	$14\sigma_p$ layers	$14\sigma_p$ layers
Horizontal advection	Walcek (Walcek and Aleksic, 1998)	PPM (Colella and Woodward, 1984)	PPM
Vertical advection	Walcek	Fully implicit backward Euler (Ramboll, 2020)	PPM
Horizontal diffusion	Multi-scale	Multi-scale	Multi-scale
Vertical diffusion	First-order K-theory (YSU-based diffusivity)	First-order K-theory (WRF/YSU-derived diffusivity; Ramboll, 2020)	ACM2 (Pleim, 2007)
Gas-phase mechanisms	CB6r5 (Yarwood et al., 2020)	CB05 (Yarwood et al., 2005)	CB6r3 (Emery et al., 2015)
Aqueous-phase chemistry	RADM (Walcek and Taylor, 1986)	RADM	AQCHEM
Aerosol processes	ISORROPIA v2.2 (Fountoukis and Nenes, 2007)	CF/ISORROPIA v1.7 (Nenes et al., 1998)	AE7/ISORROPIA v2.2
Secondary organic aerosol	Two-product model (Pandis et al., 1992; Odum et al., 1997)	SOAP2.2 (Ramboll, 2020)	AE7/VBS
Dry deposition	ZHANG03 (Zhang et al., 2001, 2003)	ZHANG03	M3DRY
Wet deposition	Henry's law (William, 1803)	Henry's law	AQCHEM
Photolysis	Full-science TUV (preprocessor) + streamlined TUV (in-model adjustment)	Full-science TUV (preprocessor) + streamlined TUV (in-model adjustment)	Binkowski et al., 2007
Boundary conditions	MORZART	Default	Default

The key configuration parameters of the EPICC-Model, CAMx, and CMAQ are summarized in Table 1. In the operational configurations adopted in this study, the EPICC-Model employs $20\sigma_z$ layers layers, whereas CMAQ and CAMx use $14\sigma_p$ layers. For vertical diffusion, the EPICC-Model employs a first-order K-theory approach based on the YSU boundary-layer parameterization. CMAQ uses the Asymmetric Convective Model version 2 (ACM2) for vertical diffusion. WRF meteorological fields generated with the ACM2 scheme are commonly used in CMAQ applications to maintain consistency in boundary-layer treatment. CAMx uses PPM for horizontal advection and a fully implicit backward Euler solver for vertical advection. Its vertical diffusion follows a first-order K-theory approach, with vertical diffusivities diagnosed from WRF meteorological fields based on the YSU parameterization. Thus, CAMx does not directly employ the complete online YSU scheme. The CB05 chemical mechanism and 14σp vertical configuration adopted in CAMx have been widely applied in regional air quality simulations, providing a reasonable balance between chemical representation, vertical resolution, and computational efficiency. Although CAMx v7.00 also supports the more recent CB6r4 mechanism, CB05 was retained because this study aims to objectively evaluate the models using their actual operational forecasting configurations during the study period, rather than to compare or optimize chemical mechanisms. The operational use of CB05 also reflects the computational-efficiency and forecast-timeliness requirements of routine forecasting, and its applicability to regional CAMx simulations over China has been demonstrated in previous studies (Wen et al., 2021). In terms of chemical mechanisms, the EPICC-Model employs the CB6r5 gas-phase mechanism coupled with RADM aqueous-phase chemistry, allowing the representation of gas-aqueous reactions contributing to secondary organic aerosol (SOA) formation, particularly under high-humidity conditions where aqueous-phase reactions can influence SOA production (Yarwood et al., 2020). The CMAQ v5.3.3 configuration used in this study employs the CB6r3 mechanism in combination with the AE7/VBS module to represent SOA formation, and from version 5.2 onward, incorporates additional parameterizations such as Potential Combustion SOA (PCSOA) to compensate for combustion-related SVOC and IVOC emissions not captured in current inventories (Murphy et al., 2017). Newer CMAQ versions include CB6r5 and its variants. CAMx uses the CB05 gas-phase chemical mechanism coupled with the SOAP module to parameterize SOA formation, simulating the oxidation of both anthropogenic and biogenic VOCs and their partitioning into the aerosol phase. For photolysis calculations, both the EPICC-Model and CAMx use the full-science TUV model as a preprocessor to generate photolysis-rate input files. A streamlined TUV module is then applied internally to adjust these rates for cloud and aerosol effects. Regarding boundary conditions, the EPICC-Model incorporates MOZART outputs as the initial and lateral background fields, while CMAQ and CAMx use their respective boundary condition preprocessing approaches. Specifically, CMAQ boundary conditions were generated based on the CB6r3 profile file, and CAMx initial and boundary conditions were prepared using the icbcprep procedure with the corresponding profile configuration, which can be found in the Zenodo repository (https://doi.org/10.5281/zenodo.17055755). These initial and lateral boundary

conditions were not harmonized across the three models, and their individual influence was not isolated through sensitivity simulations. Consequently, differences among the model results may reflect the combined effects of internal model formulations and initial and lateral boundary conditions, particularly for regional background concentrations and areas influenced by boundary inflow. These differences in physical parameterizations, chemical mechanisms, and initial and lateral boundary conditions provide important context for interpreting the differences in $PM_{2.5}$ and MDA8 O_3 simulations among the three models.

2.2 WRF model configuration and meteorological simulation evaluation

Key configuration parameters of the WRF model used in this study are summarized in Table 2. The simulations were conducted using WRF version 3.9.1, with initial and boundary conditions derived from the National Centers for Environmental Prediction (NCEP) Final 1° × 1° reanalysis data (FNL, ds083.2), featuring a temporal resolution of 6 hours. To enhance the accuracy of the WRF simulations, four-dimensional data assimilation (FDDA) grid nudging was applied during the simulation process.

Table 2. Key configuration parameters of the WRF model.

WRF v3.9.1	
Horizontal resolution	45 km-15 km (one-way nested)
Number of sigma levels	$30\sigma_p$ layers, with top layer at 50hPa
Longwave Radiation	RRTMG (Iacono et al., 2008)
Shortwave Radiation	RRTMG
Microphysics	Thompson (Thompson et al., 2008)
Land-surface Model	Unified Noah Land Surface Model (Tewari et al., 2004)
Advection	Monotonic transport
Planetary boundary layer (PBL) scheme	YSU (Hong et al., 2006)
Cumulus option	Kain-Fritsch Scheme (Kain, 2004)
Nudging options	FDDA

This study systematically evaluated the performance of the WRF model in simulating surface meteorological fields over mainland China for the year 2021, based on comprehensive observational data. The evaluation utilized daily observations from representative stations in 335 cities nationwide (excluding Jiayuguan and Wujiaqu due to data unavailability), covering key meteorological variables such as 2 m air temperature, 2 m relative humidity, 10 m wind speed, 10 m wind direction, precipitation, and surface pressure. To ensure seasonal representativeness, January, April, July, and October were selected to represent winter, spring, summer, and autumn, respectively, for comparative analysis (see Fig. S1- Fig. S24 and Supplementary Material for details, including the evaluation metrics).

The evaluation results indicate that the WRF model accurately captures the diurnal variations of key meteorological variables across most regions. For 2 m temperature simulations, the Pearson correlation coefficient (R) exceeds 0.7 in January and October,

with the Root Mean Square Error (RMSE) below 5 °C and the Mean Bias (MB) constrained within ±2 °C in North, East, and South China. Simulations of 2 m relative humidity also performed well, with R values generally above 0.7 and RMSE below 15% in April and July; MB values in East and South China were less than ± 9%. However, relatively large humidity biases were observed in parts of Southwest and Northwest China, where MB in the southwest exceeded 15% and RMSE surpassed 17%. Previous studies suggest that simulations can be considered reliable when R $\geqslant$ 0.6-0.7, RMSE for temperature $\leqslant$ 5 °C, and RMSE for humidity < 15% (Lou et al., 2025; Oyegbile et al., 2024). Therefore, the WRF model used in this study demonstrates adequacy in simulating temperature and humidity. Simulations of 10 m wind speed showed consistent performance, with R exceeding 0.7 and RMSE below 8 m/s in most regions. Nevertheless, systematic overestimations were observed in the Sichuan Basin, Xinjiang, and parts of Tibet. Although the wind speed RMSE exceeds typical values reported in some studies (4-6 m s^{-1}), it remains within an acceptable range given the seasonal variability at the national scale (Xu et al., 2020; Yu et al., 2022b). In contrast, the performance for 10 m wind direction was relatively poor, with R values below 0.4 in most areas, except for moderate improvement in the Beijing-Tianjin-Hebei region, East China, Central China, and South China. This finding aligns with previous research noting WRF's general limitations in reproducing wind direction (Jiménez and Dudhia, 2013). For precipitation, correlation coefficients were generally above 0.4 nationwide. However, substantial errors were observed in parts of Southwest, Northwest, and South China, especially in regions with complex terrain, consistent with previous findings (Yu et al., 2022a). Surface pressure simulations exhibited high consistency, with R values exceeding 0.7 across the country. While parts of Southwest and Central China exhibited slight underestimation (MB < 20 hPa), likely associated with unresolved terrain altitude differences at the model resolution, surface pressure was slightly overestimated in Guizhou and Chongqing. Overall, the WRF model provides adequate meteorological forcing fields for CTMs.

2.3 Emission inventory and observational data sources

The anthropogenic emissions data used in this study for China are derived from the Multi-resolution Emission Inventory for China (MEIC) developed by Tsinghua University, with a base year of 2019 (Geng et al., 2024). This inventory includes major source sectors such as transportation, industry, power generation, and residential combustion, and covers multiple pollutants including CO, SO_2, NOx, VOCs, PM_{10}, $PM_{2.5}$, BC, and OC. Emissions of ammonia over China are obtained from the PKU-NH_3 inventory (Huang et al., 2012a; Kang et al., 2016), while emissions from biomass burning are taken from the "China Open Biomass Burning Emissions Inventory" with a base year of 2017 (Huang et al., 2012b; Song et al., 2009). The EDGAR v5.0 dataset (Crippa et al., 2020), with a base year of 2015 and a spatial resolution of 0.1° × 0.1°, was used to represent anthropogenic emissions outside China. Biogenic emissions are simulated online using the MEGAN v3.2 model (Guenther et al., 2012). It should be noted that although the base years of the emission inventories do not match the simulation year of this study, the use of inventories from adjacent years remains a

common practice in regional air quality modeling, especially in the absence of globally consistent, high-resolution, multi-sector emission datasets for the target year. Under the assumption of no substantial changes in regional climate and socioeconomic activities, such inventories can reasonably represent the emission patterns of the study period (Amnuaylojaroen et al., 2014; Huang et al., 2023; Wang et al., 2023). It is important to clarify that no projection or temporal adjustment of the individual emission inventory data to the 2021 simulation year was performed.

All surface observational data used in this study were obtained from the China National Environmental Monitoring Center (CNEMC), including hourly $PM_{2.5}$ and O_3 concentrations from 1,644 national monitoring stations across China in 2021 (station distribution shown in Fig. S25). Based on these data, daily average $PM_{2.5}$ concentrations and MDA8 O_3 values were calculated for 337 cities. Additionally, aerosol chemical composition data were obtained from the same source for ten representative cities: Beijing (116.41°E, 40.04°N), Tianjin (117.21°E, 39.17°N), Zhengzhou (113.73°E, 34.77°N), Jinan (117.06°E, 36.66°N), Shanghai (121.53°E, 31.23°N), Nanjing (118.76°E, 32.07°N), Wuhan (114.37°E, 30.54°N), Fuzhou (119.31°E, 26.10°N), Chengdu (104.09°E, 30.64°N), and Chongqing (106.47°E, 29.62°N).

3 Results and discussion

3.1 Spatiotemporal distribution and statistical analysis of daily averages

Figure 1 presents the performance of the EPICC-Model, CAMx, and CMAQ in simulating annual $PM_{2.5}$ concentrations, evaluated against observations from 1,644 national monitoring stations across China. Based on the time series analysis (Figure 1a), the year can be divided into three distinct phases. Phase I (January to mid-May): During this period, both the EPICC-Model and CAMx significantly underestimated $PM_{2.5}$ concentrations and failed to capture the three major pollution episodes at the beginning of the year, as indicated by the circles in the figure (with biases ranging from 25 to 52 $\mu g\ m^{-3}$). In contrast, CMAQ showed improved performance in capturing both the timing and intensity of pollution peaks. This was primarily attributed to its substantially higher simulated organic carbon (OC) levels relative to the other models and observations, which produced a compensatory effect on total $PM_{2.5}$ (Figure 6). In addition, CMAQ exhibited intermittent overestimations during several periods, which may partly reflect the sensitivity of near-surface $PM_{2.5}$ concentrations to the treatment of minimum vertical eddy diffusivity (Kz_min) in ACM2, as indicated by previous CMAQ sensitivity experiments over China (Kim et al., 2024). The contrasting pattern within the rectangular box was attributed to a dust event. Phase II (mid-May to mid-October): During this period, $PM_{2.5}$ concentrations were generally low and exhibited limited variability. This was primarily attributed to elevated planetary boundary layer heights, enhanced turbulent mixing, and frequent precipitation events during the summer, which collectively facilitated the dilution and wet deposition of near-surface particulate matter. CAMx performed best in this phase. In contrast, both the EPICC-Model and CMAQ tended to overpredict pollutant levels, with CMAQ exhibiting a notably stronger positive bias. Phase III (mid-October to December): During the heating season,

observed $PM_{2.5}$ levels increased significantly, accompanied by greater spatiotemporal variability. CAMx maintained relatively good agreement with the observations, whereas the positive bias of CMAQ became more pronounced. The component evaluation in Figure 6 indicates that the substantially elevated OC concentration simulated by CMAQ was the most likely dominant contributor to this $PM_{2.5}$ overestimation, while differences in vertical mixing may have additionally influenced near-surface pollutant accumulation. The performance of the EPICC-Model was intermediate between the two.

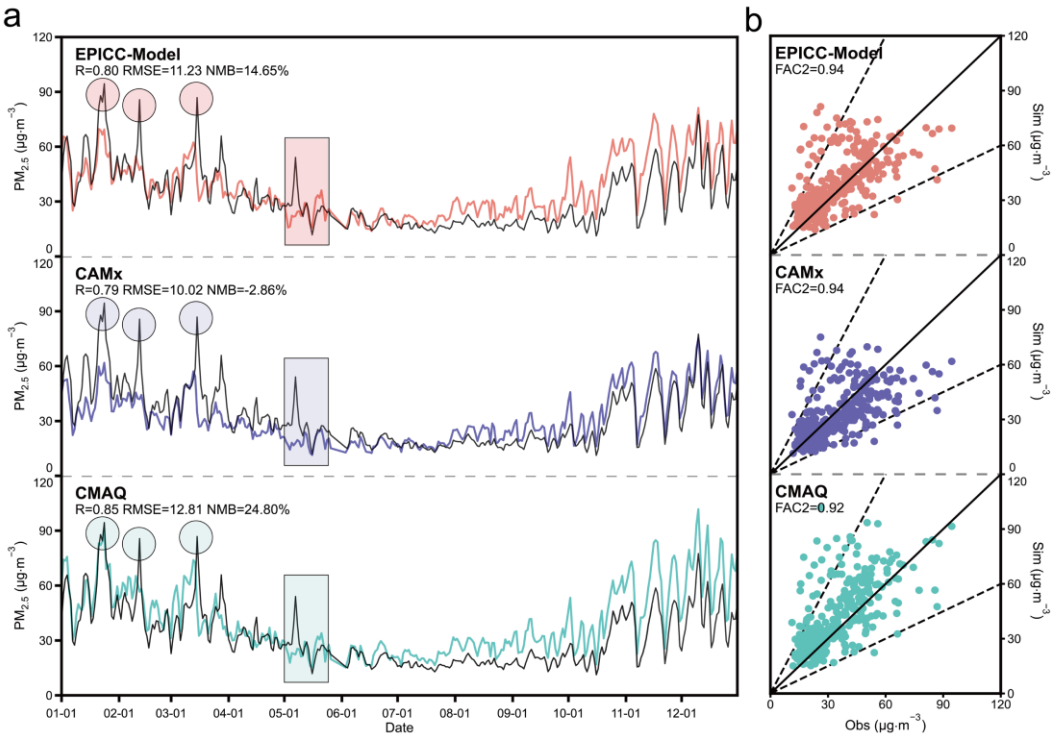

Figure 1. Comparison of simulated and observed daily $PM_{2.5}$ concentrations (i.e., daily mean $PM_{2.5}$ concentrations) across China in 2021. (a) shows the time series of daily $PM_{2.5}$, with the black line representing observations from 1,644 national air quality monitoring stations and colored lines indicating different CTMs. (b) presents scatter plots of modeled versus observed $PM_{2.5}$. All model outputs exclude dust aerosol contributions to isolate secondary particulate formation processes.

Statistical validation analysis (Figure 1b) further corroborated the above findings. Although CMAQ exhibited the highest correlation coefficient (R=0.85), most of its data points lay above the 1:1 reference line, indicating a systematic overestimation. CAMx demonstrated the best overall statistical performance, with a Fraction of Predictions Within a Factor of Two (FAC2) value of 0.94 and a Normalized Mean Bias (NMB) of merely -2.86%. It is important to note that CAMx struggles to capture severe pollution episodes, markedly underestimating periods of high concentrations, which constrains its usefulness for evaluating pollution processes. In contrast, the EPICC-Model exhibits a more pronounced seasonal response. Its simulations during spring and summer are more consistent with CAMx, indicating similar performance under the generally lower ambient $PM_{2.5}$ concentrations during these seasons, particularly in summer when enhanced boundary-layer ventilation and more frequent precipitation favor pollutant dilution and wet removal. During the autumn and winter pollution seasons, its simulation trends align more closely with CMAQ, capturing pollution accumulation processes more effectively. At the national aggregate scale represented in Figure 1, the EPICC-Model reproduced the seasonal transition of $PM_{2.5}$ concentrations and

responded to high-concentration pollution episodes while maintaining reasonably strong annual statistical performance.

Figure 2 presents the performance of the EPICC-Model, CAMx, and CMAQ in simulating MDA8 O_3 concentrations, evaluated against observations from 1,644 national monitoring stations across China. Observational data reveal a typical photochemically-driven seasonal pattern in O_3 concentrations: summer months exhibit peak levels due to enhanced VOC-NO_x chain reactions under intense solar radiation and elevated temperatures (Seinfeld and Pandis, 2016; Sillman, 1999), while O_3 concentrations remain relatively low during the colder months because weaker solar radiation suppresses photolysis and lower temperatures reduce thermochemical reaction rates, collectively weakening photochemical activity (Wang et al., 2019). The time series analysis (Figure 2a) shows that all three models reasonably reproduced the seasonal variation of O_3 concentrations, yet notable differences emerged across concentration levels. The EPICC-Model performed particularly well during high-concentration episodes, effectively capturing the peak levels of O_3 pollution. In contrast, both CAMx and CMAQ, while capable of reproducing high-concentration trends, systematically underestimated peak magnitudes with maximum negative biases reaching -20 μg m^{-3}. The improved representation of high-O_3 episodes by the EPICC-Model may be partly related to its inclusion of heterogeneous HONO formation and particulate nitrate photolysis, which can enhance radical production and O_3 formation in inland China (Bao et al., 2018; Zhang et al., 2022; Li et al., 2024). Recent EPICC-specific sensitivity and source-diagnosis studies further demonstrate that these HONO pathways, including daytime particulate nitrate photolysis, contribute to simulated HONO and O_3 formation and improve the representation of O_3 over China (Zhang et al., 2025; EPICC Model Working Group, 2026). At lower O_3 concentration levels, CMAQ reproduced the general temporal variation but exhibited a systematic positive bias, which may reflect the combined influence of vertical redistribution and photochemical production.

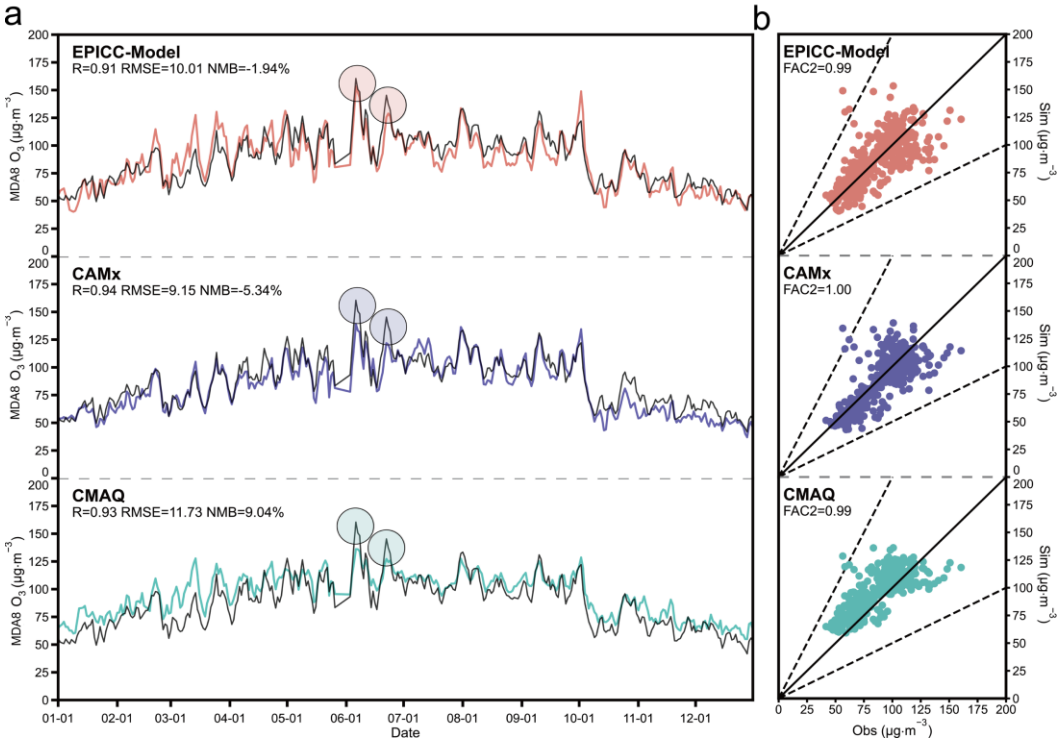

Figure 2. Comparison of simulated and observed daily MDA8 O_3 concentrations across China in 2021.

Statistical analysis indicates that CAMx achieved the highest temporal correlation (R = 0.94) and the lowest RMSE (9.15 μg m^{-3}), while exhibiting a modest negative mean bias (NMB = −5.34%). CMAQ showed a slight overestimation throughout the year but maintains a strong temporal correlation (R=0.93), demonstrating good capability in capturing temporal variations. Notably, the EPICC-Model not only accurately captured peak concentrations but also achieved the lowest annual NMB, reflecting a more robust performance overall. The scatterplots in Figure 2b show that all three models have FAC2 values close to 1, indicating comparable overall performance. The models nevertheless exhibit different statistical characteristics: CMAQ tends to overestimate MDA8 O_3, CAMx achieves the highest correlation and lowest RMSE despite a modest negative bias, and the EPICC-Model has the smallest absolute NMB.

Figure 3 compares the simulated spatial distributions of $PM_{2.5}$ for the four seasons of 2021 produced by the EPICC-Model, CAMx, and CMAQ, revealing notable differences in regional simulation consistency and bias characteristics among the three models. As shown in Figure 3, the Index of Agreement (IOA) values vary across models and seasons, exhibiting clear seasonal patterns that quantitatively support the spatial distribution differences.

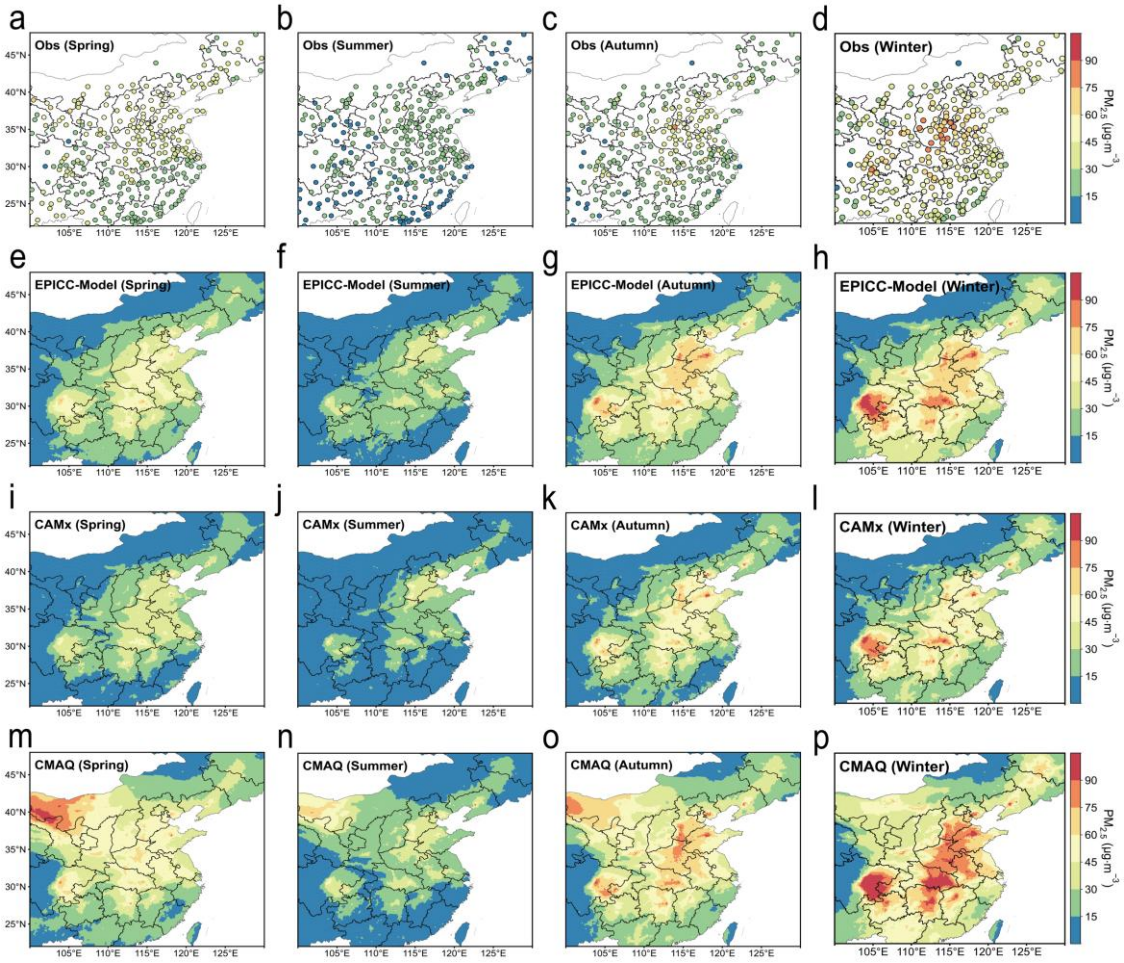

Figure 3. Seasonal spatial distributions of simulated $PM_{2.5}$ concentrations, with spring (March-May), summer (June-August), autumn (September-November), and winter (December-February).

Table 3. IOA for the spatial distribution of $PM_{2.5}$ simulated by different models.

	Spring	Summer	Autumn	Winter	Year
EPICC-Model	0.63	0.62	0.60	0.81	0.80
CAMx	0.60	0.64	0.68	0.76	0.78
CMAQ	0.72	0.58	0.54	0.73	0.77

In spring, elevated $PM_{2.5}$ concentrations occurred in several geographically separated regions, including North China, the arid basins of Northwest China, and the Sichuan Basin. This spatial pattern reflects the combined influences of northwesterly dust transport, local anthropogenic emissions, and pollutant accumulation under relatively limited ventilation in basin regions. All three models effectively reproduced the pollution pattern, with IOA values exceeding 0.60, and CMAQ achieved the highest IOA of 0.72. Since dust concentrations were excluded from the particulate matter assessment in this study, all three models consistently underestimated $PM_{2.5}$ levels in the arid Northwest and southwestern plateau regions. In summer, influenced by the southeastern monsoon and intensive precipitation, $PM_{2.5}$ remain generally low across China with reduced regional variability. The three models exhibited similar spatial consistency nationwide, with IOA values ranging between 0.58 and 0.64. However, in the high-humidity coastal regions of South China, the EPICC-Model and CMAQ demonstrated slight advantages over CAMx in simulation accuracy. In autumn, the nationwide $PM_{2.5}$ concentrations rebounded due to an increase in stagnant weather conditions and a reduced boundary layer height. All three models showed varying degrees of overestimation in North China and the Sichuan Basin, likely related to ACM2/YSU schemes underestimating mixing layer height and weakening vertical diffusion at night (Jia et al., 2023). During this period, CAMx achieved the highest IOA value of 0.68, the EPICC-Model scores 0.60, while CMAQ dropped to its annual minimum of 0.54. In winter, $PM_{2.5}$ concentrations reached their annual peak driven by low temperatures, temperature inversions, subsidence, and heating emissions. All three models successfully reproduced the pollution patterns in polluted regions like North and Central China. The EPICC-Model demonstrated exceptional performance with an IOA of 0.81, while CMAQ and CAMx maintained strong consistency at 0.73 and 0.76, respectively. However, all models unrealistically simulate higher $PM_{2.5}$ concentrations in the Sichuan Basin compared to Henan Province. This discrepancy may have resulted from differences in emission estimates between the two regions: anthropogenic emissions in the Sichuan Basin are likely overestimated in the models, whereas frequent agricultural activities in Henan may lead to underestimation of NH_3 emissions, thereby suppressing nitrate aerosol formation. Previous studies have demonstrated that spatial errors in NH_3 emissions significantly impact nitrate-driven heavy pollution events (Kang et al., 2016; Kong et al., 2019; Liu et al., 2021).

Overall, all three models reliably simulate $PM_{2.5}$ spatial distributions, with annual mean IOA values above 0.77. The EPICC-Model performs best (IOA=0.80), showing highest consistency in winter and heavily polluted North China. CAMx shows consistent performance (IOA=0.78) and is suitable for multi-seasonal averages but underestimates high-humidity regions and responds weakly to severe pollution. CMAQ shows slightly lower consistency (IOA=0.77), performs better in spring and winter,

declines in summer and autumn, and exhibits a general positive bias, particularly in winter.

Figure 4 shows the seasonal spatial distribution of MDA8 O_3 in 2021 from the three models. Given the strong seasonal variability of O_3, model performance was quantitatively evaluated using the IOA metric, with detailed results provided in Table 4.

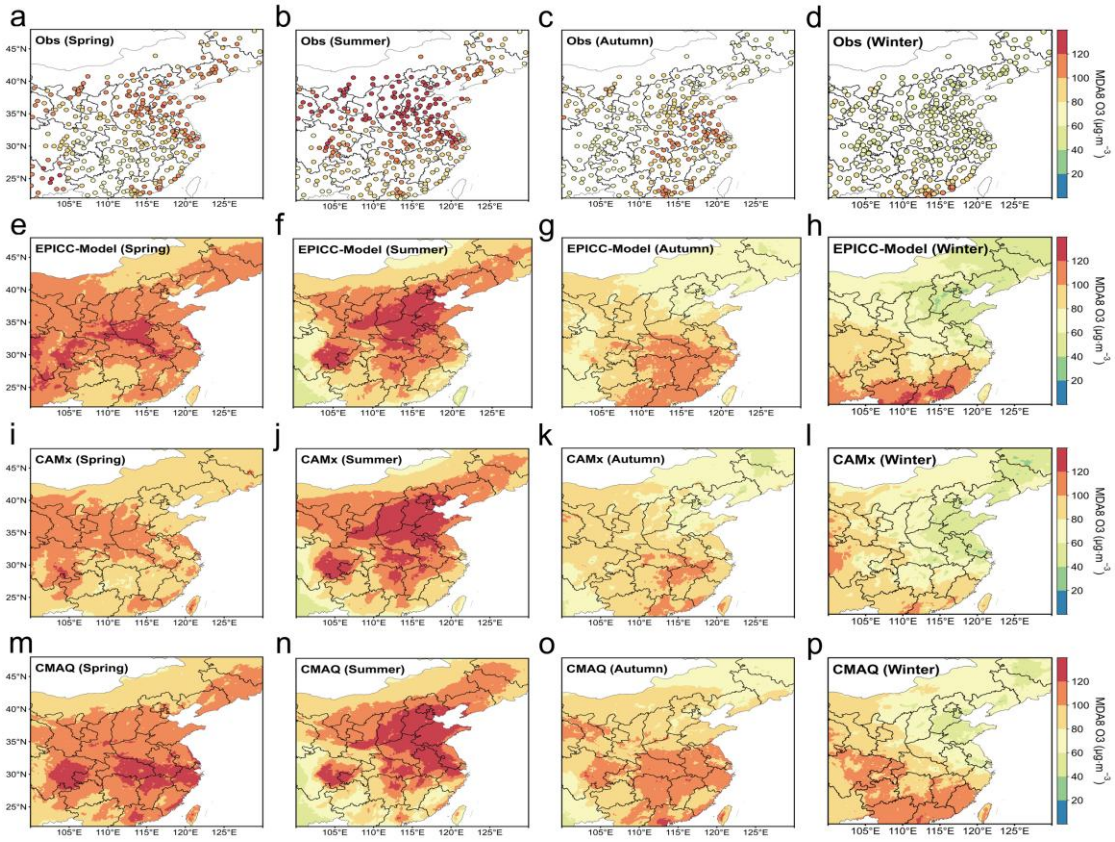

Figure 4. Seasonal spatial distributions of simulated MDA8 O_3 concentrations, with spring (March-May), summer (June-August), autumn (September-November), and winter (December-February).

Table 4. IOA for the spatial distribution of MDA8 O_3 simulated by different models.

	Spring	Summer	Autumn	Winter	Year
EPICC-Model	0.56	0.79	0.74	0.77	0.85
CAMx	0.53	0.85	0.70	0.76	0.87
CMAQ	0.33	0.85	0.78	0.75	0.84

In spring, O_3 pollution exhibits a multi-centered and scattered distribution pattern. The EPICC-Model reproduced this pattern well (IOA = 0.56) and outperformed CAMx and CMAQ, particularly in the high-concentration areas like Yunnan. CAMx generally underestimated O_3 across China, which may reflect the combined effects of its gas-phase chemistry and representation of vertical transport (Ren et al., 2022; Tang et al., 2011). CMAQ, in contrast, produced an unrealistic high-O_3 belt over the Yangtze River plain with a much lower IOA of 0.33. In summer, a high O_3 concentration belt forms over the mid-latitudes (30° N ~40° N), and all three models successfully reproduced the enhanced O_3 levels with the highest spatial consistency observed throughout the year. The summer IOA values for the EPICC-Model, CAMx, and CMAQ reach 0.79,

0.87, and 0.85, respectively. All three models were driven by meteorological inputs derived from the same WRF simulation but processed for their respective vertical structures. The simulated summer O_3 distributions therefore reflect the combined influences of regional photochemistry, meteorological transport, and lateral boundary conditions (Li et al., 2019a). In autumn, nation-wide O_3 declines as solar radiation weakens, with pollution centers shifting to eastern and southeastern coasts. All three models performed similarly (IOA 0.70–0.74). CMAQ performed best in the Pearl River Delta, accurately reproducing localized high concentrations, as supported by previous studies (Jiang et al., 2010; Wang et al., 2010). The EPICC-Model ranks second with slight overestimation in northern Jiangxi, and CAMx continues to underestimate O_3. In winter, nationwide O_3 concentrations decrease to their annual minimum, and the relative seasonal concentration maximum shifts toward southern coastal China. This redistribution reflects weaker photochemical production and stronger NO titration over northern China, whereas comparatively stronger solar radiation sustains greater photochemical activity in the south. All models perform steadily (IOA 0.75–0.77). The EPICC-Model reproduced the relative O_3 maximum over the southern coastal region, whereas CAMx displaced it farther southwest. CMAQ reproduced O_3 reasonably well over North China but overestimated concentrations mainly over the middle and lower reaches of the Yangtze River and the Sichuan Basin. These differences reflect the models' combined representations of photochemistry, NO titration, and atmospheric transport.

The evaluation indicates that the EPICC-Model shows consistent seasonal MDA8 O_3 performance with an annual IOA of 0.85, capturing O_3 distribution across China. CAMx has slightly higher consistency (IOA 0.87) but systematically underestimates in spring, autumn, and winter and misses localized peaks. CMAQ performs well in summer and autumn, especially over the Pearl River Delta, but IOA drops to 0.33 in spring and overestimates in winter, indicating a need to improve boundary layer and dry deposition schemes.

To comprehensively evaluate model performance, this study uses Taylor diagrams to compare the EPICC-Model, CAMx, and CMAQ simulations with observations on both annual and seasonal scales. The Taylor diagram simultaneously displays the correlation coefficient (R), normalized standard deviation (STD), and centered root mean square error (RMSE). In the diagram, the radial distance represents STD, the angular coordinate indicates R, and dashed contours denote RMSE relative to observations. The "REF" point (R = 1, STD = 1) represents perfect agreement with observations. The annual results (Figure 5a) show that all three models perform satisfactorily in simulating $PM_{2.5}$ and MDA8 O_3, with particularly strong performance for MDA8 O_3. Correlation coefficients exceed 0.75 for all models, while RMSE and STD remain relatively low, indicating lower variability and higher accuracy in MDA8 O_3 simulations compared to $PM_{2.5}$.

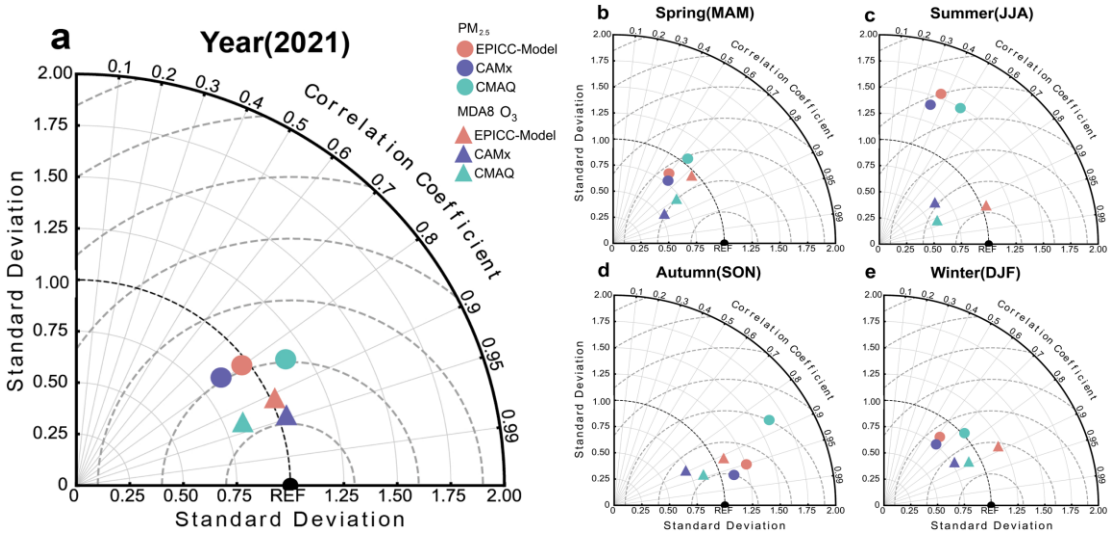

Figure 5. Taylor diagrams of $PM_{2.5}$ and MDA8 O_3 for the three models on annual and seasonal scales.

Seasonally, $PM_{2.5}$ simulation accuracy exhibits marked variations: during winter and spring high-concentration periods, all three models show comparable performance, with CMAQ demonstrating greater ability to replicate pollution peaks (STD≈1, closest to observations). Model performance declines significantly under summer's low-background conditions (R<0.55, elevated RMSE/STD), indicating enhanced error during high-concentration periods. Autumn sees performance recovery, with CAMx achieving R=0.97. In contrast, MDA8 O_3 simulations show more robust seasonal consistency: while spring remains the weakest season (R>0.7), the EPICC-Model and CMAQ maintain low errors. The EPICC-Model excels during summer O_3 peaks (R≈ 0.95, lowest RMSE/STD), CMAQ leads in autumn, and all models converge in winter (R=0.8-0.9), effectively capturing O_3 spatiotemporal patterns.

Overall, the EPICC-Model demonstrates strong robustness in seasonal O_3 simulations, maintaining consistently low standard deviations and showing clear advantages during the summer pollution peak. In contrast, CAMx and CMAQ exhibit relative strengths in $PM_{2.5}$ simulations: CAMx performs particularly well under the complex meteorological conditions of autumn, while CMAQ better captures pollutant accumulation processes during the stable boundary layer conditions in winter, reflecting their respective adaptability.

3.2 Evaluation of $PM_{2.5}$ chemical composition simulations

Based on the spatiotemporal variations of $PM_{2.5}$ total concentrations simulated by each model, the performance of the EPICC-Model, CAMx, and CMAQ in simulating major chemical components was further evaluated. Figure 6 presents the average relative contributions and absolute concentrations of key $PM_{2.5}$ components in ten representative cities across urban clusters, including the Beijing-Tianjin-Hebei, Yangtze River Delta, Chengdu-Chongqing, and the Middle Reaches of the Yangtze River regions. Overall, all three models reasonably reproduced the observed chemical composition structure characterized by a predominance of nitrate (NO_3^-), which is

consistent with previous findings (Huang et al., 2021). Observations indicated that NO_3^- accounted for approximately 31.2% to 42.4% of $PM_{2.5}$ mass in most cities. This dominant feature was reproduced by all models, although the simulated concentrations tended to be overestimated to varying degrees.

Meanwhile, all three models consistently underestimated sulfate (SO_4^{2-}), a bias consistent with existing research findings (Shao et al., 2019), which may stem from underestimating SO_2 oxidation rates or uncertainties in intra-cloud aqueous-phase chemical mechanisms. The insufficient formation of SO_4^{2-} not only limits the production of ammonium sulphate [$(NH_4)_2SO_4$] but also reduces the consumption potential of NH_3 (Gao et al., 2018), thereby suppressing the simulated concentration of ammonium (NH_4^+). The reduced formation of ammonium sulfate may also leave more NH_3 available to partition with HNO_3, potentially enhancing NH_4NO_3 formation and contributing to the overestimation of particulate NO_3^- in some regions.

For OC, although certain deviations are observed in individual cities, the overall simulation performance of the three models remains within an acceptable range (Miao et al., 2020). Among them, the EPICC-Model and CAMx produced results that are closer to observations, while CMAQ tends to systematically overestimate OC concentrations. This systematic bias may stem from the introduction of Potential Combustion SOA (PCSOA) species starting from CMAQv5.2. PCSOA serves as a surrogate secondary organic aerosol species to compensate for the lack of combustion-related SVOC and IVOC emissions in current inventories. However, the model estimates PCSOA concentrations through parameterized precursor emissions and simplified processes including OH oxidation and gas-particle partitioning. The associated uncertainties may result in regional and temporal discrepancies, failing to reflect the real-world variations in PCSOA and consequently leading to simulation biases (Murphy et al., 2017; Pennington et al., 2021). Overall, all three models share substantial uncertainties in SOA-related mechanisms, representing a common limitation.

Black carbon (BC) is the least abundant component of $PM_{2.5}$, with observed concentrations ranging from 0.7 to 2.1 μg m^{-3}. All models exhibit generally consistent performance in simulating its relative contribution, with slight overestimations observed in Beijing, Tianjin, and Zhengzhou. In Beijing and Zhengzhou, the elevated fractions are accompanied by overestimated absolute BC concentrations, suggesting possible uncertainties in BC emission magnitude or spatial allocation, as well as in mixing, transport, and removal processes. In Tianjin, however, the absolute BC bias is small, and the elevated fraction mainly results from underestimation of the total measured-component concentration. Differences in spatial representativeness between individual urban sites and grid-cell-averaged concentrations may introduce additional uncertainty, although their influence on the direction of the bias cannot be determined from the available data (Hong et al., 2017).

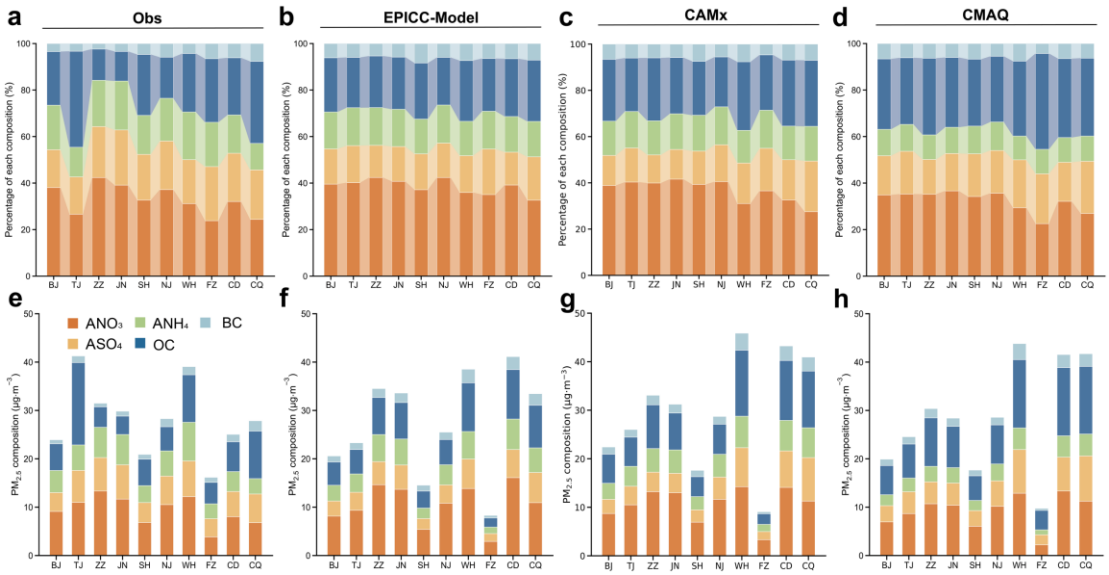

Figure 6. Comparison of simulated and observed aerosol components in representative Chinese cities. ASO_4, ANO_3, ANH_4, OC, and BC denote sulfate, nitrate, ammonium, organic carbon, and black carbon in $PM_{2.5}$, respectively. The locations of monitoring sites are as follows: BJ (Beijing; 116.41° E, 40.04° N), TJ (Tianjin; 117.21° E, 39.17° N), ZZ (Zhengzhou; 113.73° E, 34.77° N), JN (Jinan; 117.06° E, 36.66° N), SH (Shanghai; 121.53° E, 31.23° N), NJ (Nanjing; 118.76° E, 32.07° N), WH (Wuhan; 114.37° E, 30.54° N), FZ (Fuzhou; 119.31° E, 26.10° N), CD (Chengdu; 104.09° E, 30.64° N), and CQ (Chongqing; 106.47° E, 29.62° N).

As shown in the stacked bar charts of $PM_{2.5}$ absolute concentrations in Figure 6e-6h, Tianjin exhibits the highest levels among the selected cities, followed by Wuhan, while Fuzhou shows the lowest. This spatial pattern is closely related to regional emission intensity and meteorological conditions. The three models reasonably reproduce these concentrations in most cities, particularly in Nanjing. However, systematic biases exist in certain locations. Simulated concentrations in Tianjin are substantially lower than observations, primarily due to underestimation of OC associated with uncertainties in SOA formation mechanisms. In contrast, concentrations in Chengdu and Chongqing are consistently overestimated across all models, indicating an amplified model response to pollution episodes in central China. Overall, while the models capture the major chemical composition features, their ability to accurately reproduce absolute concentrations and regional variability remains limited, highlighting the need for refined emission inventories and improved representation of meteorological processes.

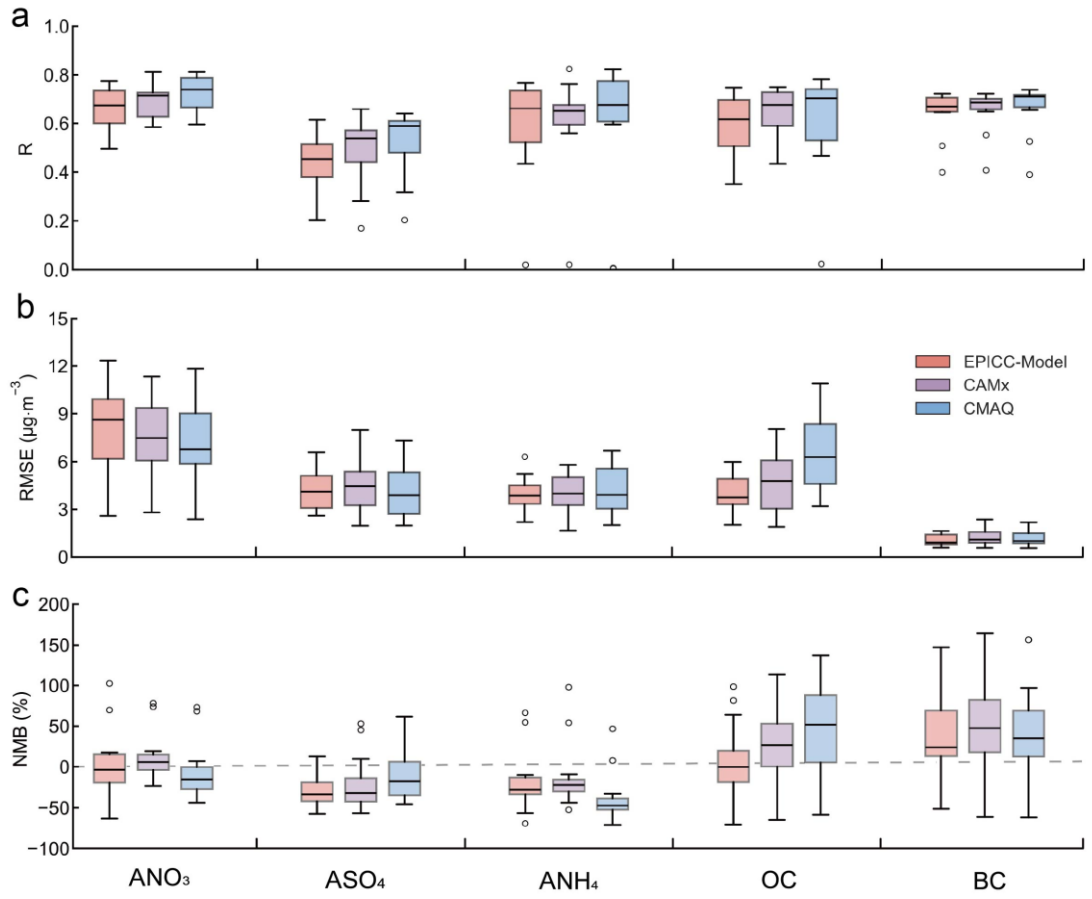

Figure 7. Performance metrics of aerosol component simulations across models in representative Chinese cities.

Figure 7 presents boxplots of statistical evaluation metrics (R, RMSE, and NMB) based on ten representative cities to quantify the simulation accuracy and systematic biases of each model. Regarding the overall distribution of R values, a clear "stepwise" difference is observed among the three models. CMAQ generally exhibits higher R values across $PM_{2.5}$ components than the EPICC-Model and CAMx, indicating stronger capability in reproducing spatiotemporal variability. Among individual components, NO_3^- shows the highest correlation (median $R > 0.6$) with no outliers, suggesting robust representation. NH_4^+ and OC display slightly lower R values, reflecting moderate uncertainty but acceptable overall performance. SO_4^{2-} shows dispersed correlations and some low R values, indicating substantial simulation errors, likely due to insufficient representation of regional secondary aerosol formation. BC exhibits the most compact R distribution, with low inter-city variability, reflecting robust and consistent simulation by all models. The RMSE analysis shows larger errors for NO_3^- and OC, with some cities reaching 12 μg m^{-3} and median values above 6 μg m^{-3}, reflecting sensitivity to meteorology, secondary processes, and SOA-related uncertainties. The EPICC-Model performs well in this aspect. SO_4^{2-} and $NH4^+$ exhibit moderate RMSE, indicating relatively low variability simulations, while BC shows the lowest RMSE and most compact distribution, suggesting high accuracy. The NMB results show that the deviations of NO_3^-, SO_4^{2-}, and NH_4^+ are relatively constrained, although overestimations or underestimations still occur in some cities. In contrast, the NMB

boxplots for OC and BC exhibit significant elongation, with deviations ranging from -50% to +150% in certain locations. The high bias of OC is mainly attributed to inaccuracies in the representation of SOA formation and precursor emissions, while the large relative deviations of BC are likely due to its low ambient concentrations, where even minor absolute errors can lead to amplified relative discrepancies.

A cross-model comparison reveals that CMAQ exhibits the highest correlation coefficients, particularly excelling in reproducing the spatial and temporal patterns of NO_3^- and NH_4^+. However, it shows a tendency to overestimate OC concentrations. CAMx shows intermediate performance across most components. The performance of the EPICC-Model varies among chemical components and cities, with its RMSE and NMB generally falling within the ranges of the other two models.

3.3 AQI and pollution forecast accuracy

To benchmark the performance of the three CTMs across air-quality categories, we evaluated the categorical forecasts of the EPICC-Model, CAMx, and CMAQ following the *Technical guideline for numerical forecasting of ambient air quality* (HJ1130-2020) and the *Technical Regulation for the Assessment of Urban Ambient Air Quality Index (AQI) Forecasts (Trial)* (China National Environmental Monitoring Center, 2020). For the Air Quality Index (AQI) level evaluation, an AQI interval from 0.75F to 1.25F was first constructed, where F denotes the forecast AQI. This interval was converted to the corresponding air-quality-level range, and a forecast was considered correct when the observed level fell within that range. Missing observations or simulations were excluded before classification and evaluation. $PM_{2.5}$ and MDA8 O_3 were also evaluated separately using their respective IAQI categories. Because the present model configurations do not include wind-blown dust emissions, the combined heavy/severe $PM_{2.5}$ category is retained as a diagnostic evaluation of model performance under the configurations used in this study, rather than as an evaluation of dust-forecasting capability. To determine whether the statistics for this category were dominated by typical dust events, the spatial and seasonal distribution of the observed heavy/severe $PM_{2.5}$ events was additionally examined. The detailed analysis is presented in Section S4 and Table S1 of the Supplement. Overall, the categorical forecast accuracy generally decreased as the observed pollution level increased. The algorithms and definitions of AQI and IAQI are provided in the Supplementary Material for reference.

In terms of overall forecasting accuracy, CAMx performed best for AQI, $PM_{2.5}$ IAQI, and MDA8 O_3 IAQI, with accuracies of 84%, 83%, and 90%, respectively. The EPICC-Model showed competitive performance in several light and moderate pollution categories. This performance is physically consistent with the heterogeneous pathways represented in the model, including manganese-catalyzed SO2 oxidation, N_2O_5 heterogeneous hydrolysis, and heterogeneous HONO formation (Wang et al., 2021; Zhang et al., 2022; Yang et al., 2024; EPICC-Model Working Group, 2026). For $PM_{2.5}$, CMAQ showed the highest accuracy in the moderate and combined heavy/severe categories, reaching 61% and 40%, respectively. Nevertheless, all three models showed substantially lower accuracy in the combined heavy/severe $PM_{2.5}$ category than in the

lower pollution categories.

Table 5. Comparison of AQI level forecast accuracy for 337 Chinese cities.

Model	Excellent	Good	Light Pollution	Moderate Pollution	Heavy/Severe Pollution	Accuracy
EPICC-Model	85%	85%	62%	39%	23%	82%
CAMx	90%	87%	57%	31%	11%	84%
CMAQ	83%	88%	63%	41%	36%	82%

Table 6. Comparison of $PM_{2.5}$ IAQI level forecast accuracy at 1,644 monitoring sites in China with observations.

Model	Excellent	Good	Light Pollution	Moderate Pollution	Heavy/Severe Pollution	Accuracy
EPICC-Model	88%	74%	66%	51%	25%	82%
CAMx	92%	69%	57%	40%	13%	83%
CMAQ	86%	75%	66%	61%	40%	82%

Table 7. Comparison of MDA8 O_3 IAQI level forecast accuracy at 1,644 monitoring sites in China with observations.

Model	Excellent	Good	Light Pollution	Moderate Pollution	Heavy/Severe Pollution	Accuracy
EPICC-Model	92%	84%	67%	47%	10%	88%
CAMx	97%	81%	66%	44%	17%	90%
CMAQ	89%	91%	72%	35%	10%	88%

Given the high sensitivity and risk posed by polluted weather and severe pollution events to public health and environmental management, this study further focuses on the forecasting performance of $PM_{2.5}$ and MDA8 O_3 pollution events. Based on metrics such as hit rate, false alarm rate, and the distance from the random operating characteristic (DROC) (definitions and calculation methods are provided in the Supplementary Material), the forecast effectiveness for general pollution conditions ($PM_{2.5} > 75$ μg m^{-3} and MDA8 $O_3 > 160$ μg m^{-3}) and severe pollution conditions ($PM_{2.5} >$ 150 μg m^{-3}) is thoroughly analyzed to elucidate the applicability and potential limitations of each model under extreme pollution scenarios.

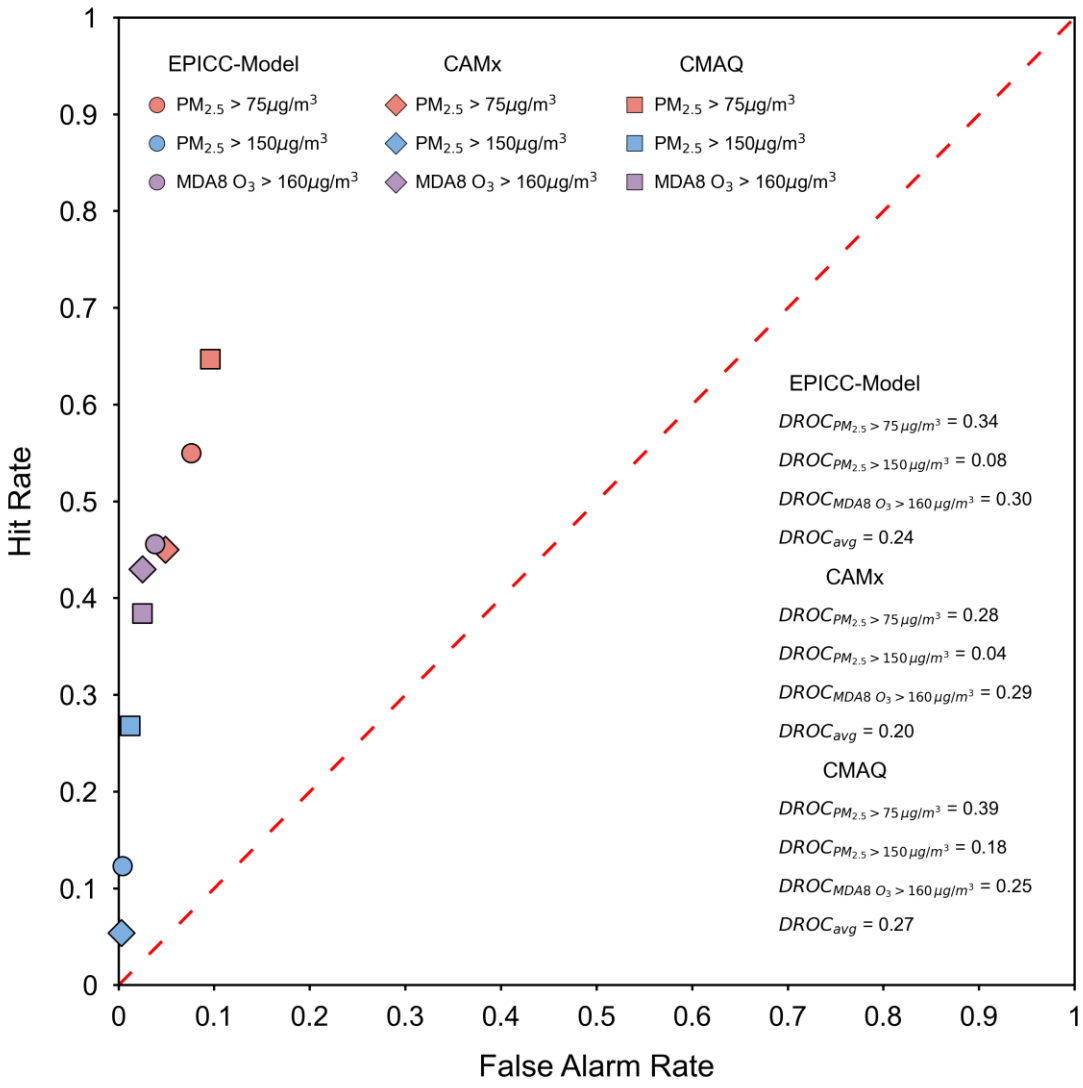

Figure 8. Comparison of CTMs performance based on hit rate and false alarm rate. Scatter points represent the performance of three models (EPICC-Model: circles, CAMx: diamonds, CMAQ: squares) under different pollution event thresholds: $PM_{2.5}$ > 75 μg m^{-3}, $PM_{2.5}$ > 150 μg m^{-3}, and MDA8 O_3 > 160 μg m^{-3}. The red dashed line indicates the random forecast reference line. The DROC metric, which quantifies model skill, is provided in the lower-right corner, with higher values indicating better model performance.

Figure 8 visually compares the forecast performance of three models under different pollution thresholds using scatter points in ROC space. For general pollution scenarios ($PM_{2.5}$ > 75 μg m^{-3}), CMAQ shows the highest hit rate (64.7%) but is accompanied by a relatively high false alarm rate (9.6%), indicating a tendency toward systematic overestimation. CAMx achieves the lowest false alarm rate (4.9%), likely because it tends to underpredict $PM_{2.5}$ levels and forecast fewer high pollution events. However, its hit rate is also relatively low (45.0%), reflecting a more conservative forecasting tendency. The EPICC-Model strikes a balance between hit rate (55.0%) and false alarm rate (7.6%), suggesting a trade-off between detection capability and false alarm occurrence. Under the more severe pollution condition ($PM_{2.5}$ > 150 μg m^{-3}), the hit rates of all models decrease significantly. While CMAQ still maintains the highest

hit rate (26.8%), its miss rate reaches 73.2%. The EPICC-Model and CAMx show hit rates of only 12.3% and 5.4%, respectively, indicating limited responsiveness of current models to extreme pollution events. Nevertheless, all models maintain false alarm rates below 2%. This reflects limitations of the models in simulating extreme pollution conditions. For O_3 pollution events (MDA8 O_3 > 160 μg m^{-3}), the EPICC-Model achieves the highest hit rate (45.6%), slightly higher than CAMx (43.0%) and CMAQ (38.4%), while also maintaining a low false alarm rate (3.8%). The DROC values provided in the lower-right table quantitatively reflect the above observations: CMAQ has the highest DROC (0.39) for general $PM_{2.5}$ pollution events, while the EPICC-Model performs best for O_3 events (DROC=0.30). CAMx exhibits relatively low DROC across all thresholds.

3.4 Capability in capturing regional persistent pollution events

To further evaluate the capability of the EPICC-Model, CAMx, and CMAQ in simulating trans-regional and long-duration pollution episodes, this study selects typical persistent $PM_{2.5}$ and O_3 events in 2021, and conducts a dedicated analysis incorporating pollutant transport pathways and the spatiotemporal consistency of meteorological fields.

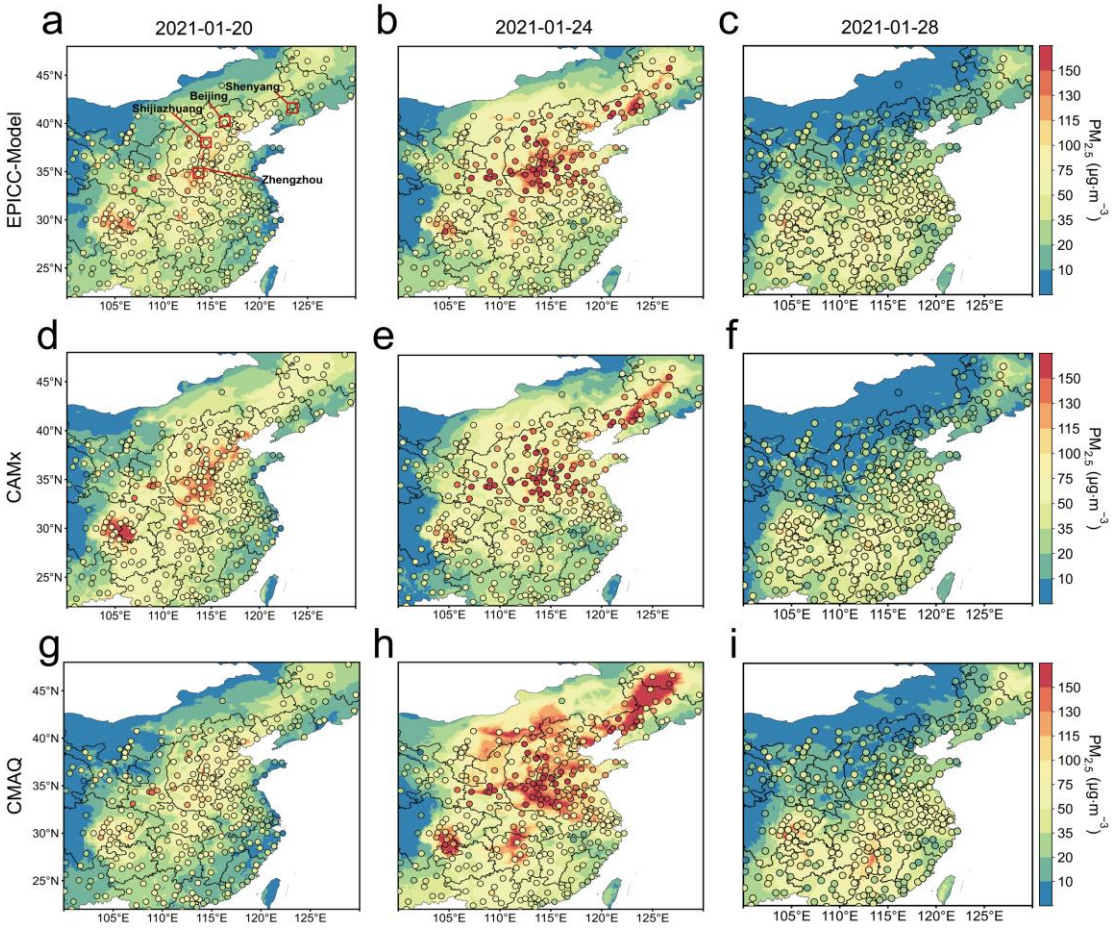

Figure 9. Spatiotemporal distribution of the persistent $PM_{2.5}$ pollution event. Dots represent observed concentrations in 377 cities.

As shown in Figure 9, a persistent $PM_{2.5}$ pollution event occurred in eastern and central China from January 20 to 28, 2021. Initially, pollution was concentrated between 30° N and 40° N, forming a "dual-core" pattern over the North China Plain and the Sichuan Basin. By January 24, $PM_{2.5}$ concentrations peaked, with the pollution belt extending southeastward to the middle and lower Yangtze River regions and northeastward to the Songnen Plain. On January 28, under cold air influence, concentrations dropped below 75 μg m^{-3} in most areas, leaving only isolated hotspots. All three models captured the temporal evolution from initiation to dissipation. The EPICC-Model showed better performance in reproducing spatial gradients and temporal patterns, particularly in the centre of the North China Plain and Yangtze River Middle-Reach corridor. CAMx reproduced the northeastward transport path but underestimated pollution intensity, failing to capture the strong core in Henan during the peak. CMAQ systematically overestimated concentrations.

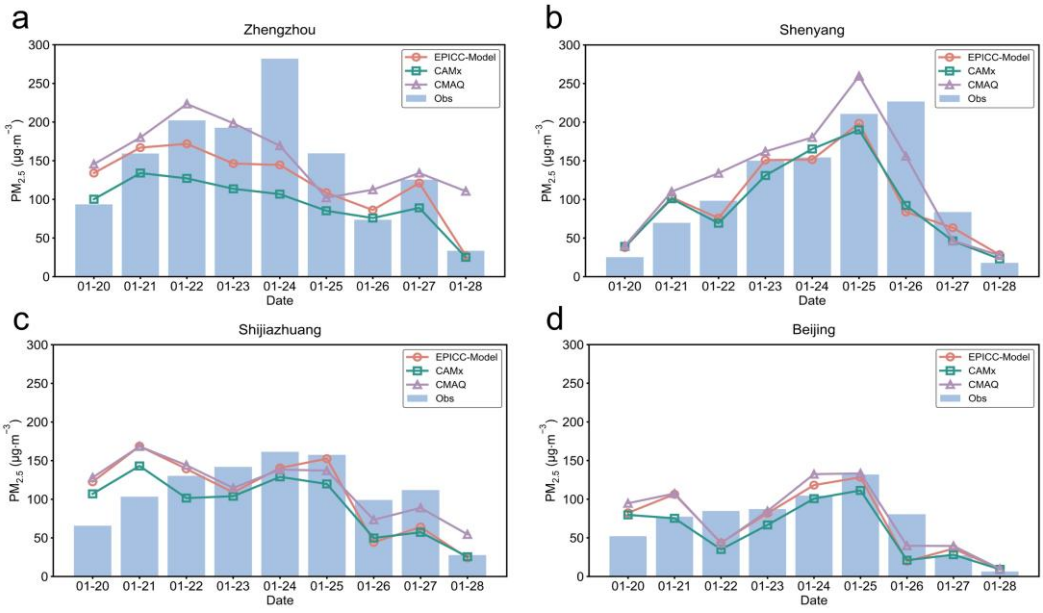

Figure 10. Time series of $PM_{2.5}$ concentrations in key cities along the pollution belt.

As shown in Figure 10, Zhengzhou recorded the first $PM_{2.5}$ peak (>150 μg m^{-3}) on January 21, with the pollution plume spreading northeastward and causing a delayed concentration rise in Shenyang. All four cities (Zhengzhou, Shenyang, Shijiazhuang, and Beijing) reached their maxima, though peak timings varied. During the clearing phase, driven by southward cold air intrusion, concentrations declined across all cities, with faster removal in Zhengzhou and Shijiazhuang than in Shenyang and Beijing. All three models reproduced the overall process but showed systematic timing biases, with peaks in Shenyang and Zhengzhou simulated 24-48 hours earlier than observed. Such deviations may result from inaccuracies in the simulated wind field evolution within the meteorological models. In terms of magnitude, CAMx underestimated and CMAQ overestimated concentrations in Zhengzhou, while the EPICC-Model produced comparatively robust results. In the other three cities, all models tracked concentrations similarly.

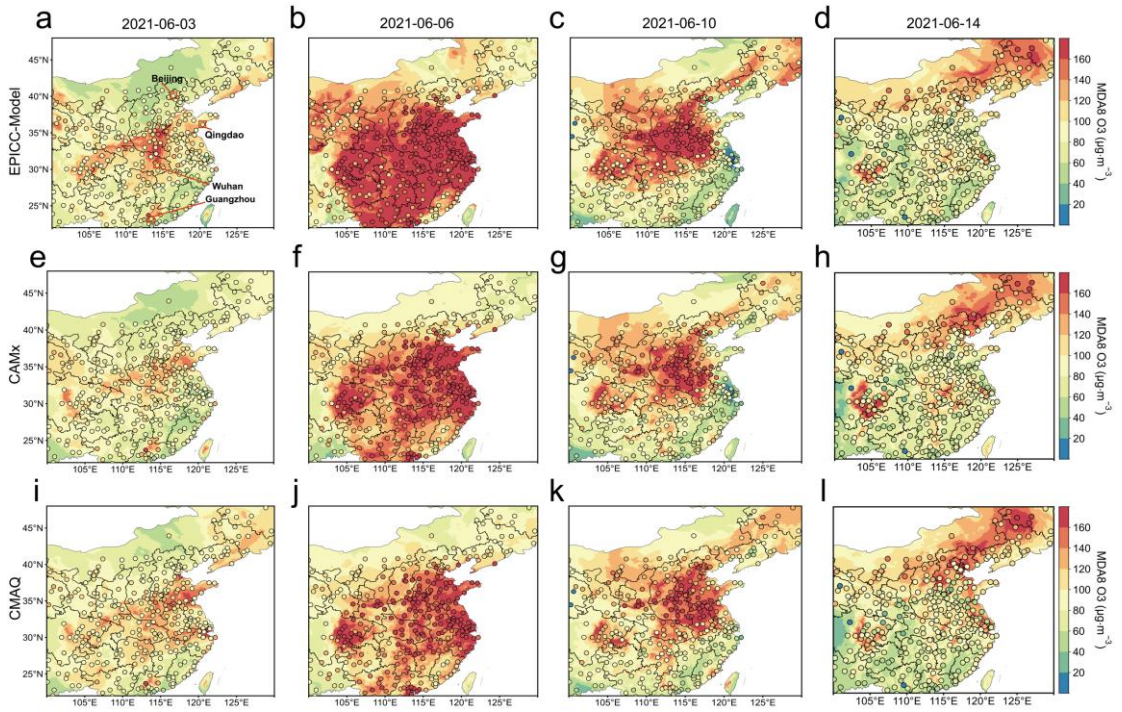

Figure 11. Spatiotemporal distribution of the persistent O_3 pollution event.

As shown in Figure 11, a persistent O_3 pollution episode occurred in China from June 3 to 14, 2021. The event began on June 3 with scattered pollution over the North China Plain and parts of Guangdong Province. By the peak stage on June 6, pollution intensity increased significantly, spreading to central, southeastern, and southern regions. By June 10, the pollution weakened and became more localized in North China and its western areas, while southern regions began clearing. By June 14, MDA8 O_3 concentrations dropped below 100 μg m^{-3} across most areas, leaving only a few localized hotspots in Northeast China and Inner Mongolia. Elevated temperatures, strong solar radiation, and stagnant atmospheric conditions favored O_3 formation, whereas cold air intrusions promoted dispersion and removal.

During this persistent pollution event, all three models captured the full process of occurrence, development, and removal. The EPICC-Model reproduced the expansion of the elevated-O_3 area from central China toward southeastern and southern China and the subsequent clearing, although it locally overestimated O_3 over southeastern China during the peak stage on 6 June, potentially reflecting uncertainties in simulated photochemistry and regional transport. CAMx and CMAQ generally underestimated O_3 in the observed high-concentration regions, particularly on 6 and 10 June, but reproduced the local contrasts between neighboring high-O_3 and low-O_3 monitoring sites more clearly. In comparison, the EPICC-Model reproduced a broader region of elevated O_3 but produced a smoother and more spatially extensive enhancement, resulting in local overestimation in parts of central and southeastern China. Overall, the EPICC-Model showed an advantage in representing the regional extent of the elevated-O_3 area during this episode.

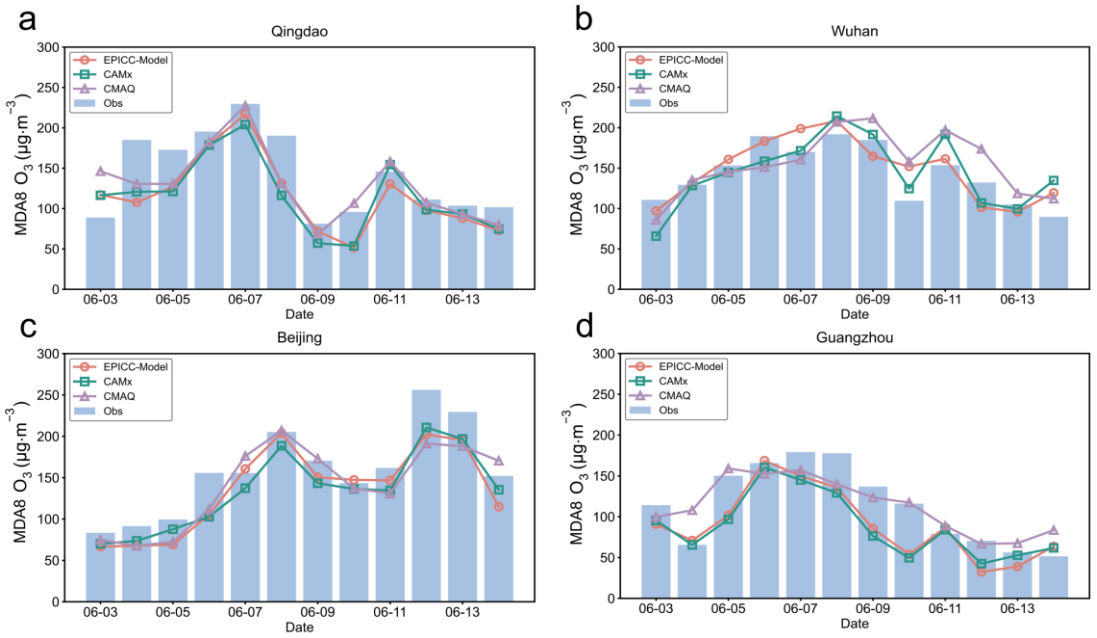

Figure 12. Time series of O_3 concentrations in key cities along the pollution belt.

The pollution event occurred over central and eastern China between 30° N and 40° N. Qingdao first entered O_3 pollution on June 4, with MDA8 O_3 exceeding 160 μg m^{-3}. The pollution then maintained high concentrations and expanded northward and southward, reaching Qingdao, Wuhan, Beijing, and Guangzhou by June 6. After June 9, the first clearing phase began from south to north, with Guangzhou improving first, followed by Wuhan and Qingdao, while the pollution center shifted to the North China Plain and northeastern regions, causing a sharp rise in Beijing around June 12. By June 14, most regions had cleared, with Beijing showing the fastest decline, likely due to enhanced cold air activity and higher boundary layer. All three models captured the full progression in Beijing and Qingdao accurately. For Wuhan and Guangzhou, model predictions showed approximately one-day deviations from observations, likely due to limited responses to abrupt meteorological changes.

4 Conclusions

This study presents a systematic evaluation of three CTMs (EPICC-Model, CAMx, and CMAQ) for $PM_{2.5}$ and MDA8 O_3 simulations over China in 2021, using meteorological fields derived from the same WRF simulation and multi-source emission inventories. The work fills a critical research gap by providing the first comprehensive comparison of the EPICC-Model against established CTMs. The results indicate that all three models can effectively reproduce the spatiotemporal evolution characteristics of $PM_{2.5}$ and MDA8 O_3 ($PM_{2.5}$: R = 0.79-0.85, MDA8 O_3: R = 0.91-0.94). The $PM_{2.5}$ bias of the EPICC-Model varies seasonally, with a tendency toward underestimation in spring and summer and overestimation in autumn and winter. Spatially, it exhibits higher consistency (annual IOA = 0.80), particularly in winter and over heavily polluted North China, effectively capturing pollution patterns and peaks. For O_3, the EPICC-Model performs well during high-concentration summer episodes,

and this performance may be partly associated with its inclusion of heterogeneous HONO formation and particulate nitrate photolysis. Furthermore, the EPICC-Model produces particularly accurate O3 simulations over the eastern, central, and Chengdu-Chongqing regions. Notably, all three models share common deficiencies in $PM_{2.5}$ simulations. Systematic underestimations occur in arid northwestern China due to unaccounted dust processes, highlighting the critical influence of natural emissions on model accuracy. Conversely, autumn-winter $PM_{2.5}$ overestimations occur in North China and the Sichuan Basin. Insufficient nocturnal mixing may contribute to these biases, consistent with previously reported tendencies of the ACM2/YSU boundary-layer schemes under stable conditions (Jia et al., 2023). Uncertainties in emission inventories further exacerbate regional biases, such as potential overestimation of anthropogenic emissions in the Sichuan Basin and underestimation of agricultural NH_3 emissions in Henan, which affects nitrate aerosol formation. Future improvements should incorporate dust processes, refine boundary layer parameterizations to better simulate pollutant accumulation under stable meteorological conditions, and employ higher-resolution emission inventories with improved temporal variability characterization.

In terms of $PM_{2.5}$ component simulations, the EPICC-Model, CAMx, and CMAQ all reasonably reproduce the chemical composition characterized by NO_3^- dominance and associated regional variations. Compared with CAMx and CMAQ, the EPICC-Model exhibits smaller biases in SO_4^{2-} and NH_4^+, with more robust control of absolute concentrations as reflected in RMSE and NMB, indicating a relatively consistent overall performance, although its correlation metrics are slightly lower than the other two models. Nevertheless, all three models share common limitations: SO_4^{2-} is generally underestimated, leading to insufficient formation of $(NH_4)_2SO_4$ and lower NH_4^+ concentrations; SOA formation remains highly uncertain, influenced by precursor VOC emissions, oxidation pathways, and gas-particle partitioning parameterizations, resulting in spatial deviations in OC; BC simulations are highly sensitive to emission inventories, occasionally leading to slight overestimations in certain cities. Addressing these issues in future work should focus on optimizing secondary inorganic aerosol chemistry, improving SOA formation mechanisms and precursor emissions, and enhancing the resolution and accuracy of emission inventories to improve the models' capability in reproducing $PM_{2.5}$ chemical composition.

Regarding AQI level classification ability, CAMx achieved the highest overall accuracy (84%), demonstrating particular strengths in distinguishing "excellent" and "good" air quality levels. CMAQ is relatively accurate in pollution level identification, with the highest hit rate (64.7%) in forecasting general pollution where $PM_{2.5} > 75$ μg m^{-3}, but it has a high false alarm rate (9.6%), indicating a tendency toward over-forecasting. The EPICC-Model shows higher hit rates in forecasting $PM_{2.5}$ light to moderate pollution levels and MDA8 O_3 general pollution, achieving 45.6% for MDA8 $O_3 > 160$ μg m^{-3}, compared with 43.0% for CAMx and 38.4% for CMAQ. For severe $PM_{2.5}$ pollution events exceeding 150 μg m^{-3}, all three models showed low hit rates, ranging from 5.4% to 26.8%, although their false alarm rates remained below 2%. In addition, the EPICC-Model demonstrated relatively balanced false alarm rates across

all pollution types, suggesting a simulation capability comparable to other mainstream models and particular effectiveness in capturing light to moderate pollution and O_3 pollution.

In the simulation analysis of typical persistent $PM_{2.5}$ and O_3 pollution events in 2021, the EPICC-Model demonstrated strong capabilities, particularly outperforming CAMx and CMAQ in reproducing spatial distributions and pollution evolution. The EPICC-Model successfully captured the entire process of pollution occurrence, development, and clearance, particularly in the core area of the North China Plain and the diffusion zone of the middle Yangtze River, where the simulation results were in close agreement with observational data. CAMx and CMAQ, however, performed less effectively in capturing persistent pollution events, both exhibiting significant deviations during the simulation of severe pollution phases. CAMx tended to underestimate pollution intensity during some high-concentration stages, while the models exhibited timing deviations during the development or dissipation of individual episodes.

This study establishes a multi-model evaluation framework for systematically comparing the performance of the EPICC-Model with established CTMs over China. By identifying model-specific limitations and challenges shared across the three models, the comparison highlights priorities for future model development, including improved representations of natural dust, boundary-layer mixing, secondary aerosol formation, and emission inputs. The results provide benchmark information for evaluating, selecting, and further developing regional air-quality modeling systems in China. The multi-model evaluation framework and identified performance characteristics may also serve as a reference for model applications in other regions facing similar air-quality modeling challenges.

Code and data availability

All models used in this study are open source and publicly available. The EPICC-Model v1.0 source code is archived at https://doi.org/10.5281/zenodo.20303367. CAMx v7.00 can be downloaded from https://www.camx.com/download/source/ (Ramboll, 2020), while CMAQ v5.3.3 is available through https://doi.org/10.5281/zenodo.5213949. Meteorological fields were generated using the WRF v3.9.1 (Skamarock et al., 2008), which is available from https://www2.mmm.ucar.edu/wrf/users/download/get_source.html. Initial and boundary conditions were derived from the NCEP FNL reanalysis dataset (NCEP, 2000), archived at https://doi.org/10.5065/D6M043C6. Anthropogenic emissions over China were obtained from the MEIC inventory developed by Tsinghua University (Geng et al., 2024), available at http://meicmodel.org.cn/?page_id=541&lang=en. Chinese NH_3 emissions were taken from the PKU-NH_3 inventory, while biomass-burning emissions were obtained from the China Open Biomass Burning Emissions Inventory (Huang et al., 2012a, 2012b; Song et al., 2009; Kang et al., 2016). Both datasets are available through the MEIC data platform at http://meicmodel.org.cn/?page_id=1772&lang=en. Emissions outside China were represented using the EDGAR v5.0 inventory (Crippa et al., 2020), available at

https://edgar.jrc.ec.europa.eu/dataset_ap50. Biogenic emissions were calculated online using MEGAN v3.2, whose source code is archived at https://zenodo.org/records/10526206 (Guenther et al., 2012). Air quality observations were obtained from the China National Environmental Monitoring Centre (CNEMC; https://www.cnemc.cn/). The primary datasets generated and analysed in this study, as well as the emission data employed (using the 15th of each month as an example), are available in Zenodo at https://doi.org/10.5281/zenodo.20843312. Additional supporting materials are available from the corresponding author upon reasonable request.

Author contributions

ML, QW, WengdW, and HC conceptualized and organized the study. ML performed the data analysis and drafted the manuscript. ML and XF conducted the numerical simulations, and FY optimized the simulation code. XF and WeiW provided data support. DL contributed to the meteorological model evaluation. ML, QW, WengdW, and HC validated and analyzed the simulation results. KC, JZ, and ZW reviewed the research findings and provided key feedback. All authors read and approved the final manuscript.

Competing interests

The authors declare no competing interests.

Acknowledgements

We appreciate the technical support provided by the National Large Scientific and Technological Infrastructure, the "Earth System Numerical Simulation Facility" (https://cstr.cn/31134.02.EL).

Financial support

This study was supported by the National Key Research and Development Program of China (Grant No. 2023YFC3705705 and 2024YFC3713603) and the Strategic Priority Research Program of the Chinese Academy of Sciences (Grant No. XDB0760400).

Reference

Amnuaylojaroen, T., Barth, M. C., Emmons, L. K., Carmichael, G. R., Kreasuwun, J., Prasitwattanaseree, S., and Chantara, S.: Effect of different emission inventories on modeled ozone and carbon monoxide in Southeast Asia, Atmos Chem Phys, 2014.

Appel, K. W., Napelenok, S. L., Foley, K. M., Pye, H. O. T., Hogrefe, C., Luecken, D. J., Bash, J. O., Roselle, S. J., Pleim, J. E., Foroutan, H., Hutzell, W. T., Pouliot, G. A., Sarwar, G., Fahey, K. M., Gantt, B., Gilliam, R. C., Heath, N. K., Kang, D., Mathur, R., Schwede, D. B., Spero, T. L., Wong, D. C., and Young, J. O.: Description and evaluation of the Community Multiscale Air Quality (CMAQ) modeling system version 5.1, Geosci. Model Dev., 10, 1703–1732, https://doi.org/10.5194/gmd-10-1703-2017, 2017.

Appel, K. W., Bash, J. O., Fahey, K. M., Foley, K. M., Gilliam, R. C., Hogrefe, C., Hutzell, W. T.,

Kang, D., Mathur, R., Murphy, B. N., Napelenok, S. L., Nolte, C. G., Pleim, J. E., Pouliot, G. A., Pye, H. O. T., Ran, L., Roselle, S. J., Sarwar, G., Schwede, D. B., Sidi, F. I., Spero, T. L., and Wong, D. C.: The Community Multiscale Air Quality (CMAQ) model versions 5.3 and 5.3.1: system updates and evaluation, Geosci. Model Dev., 14, 2867–2897, https://doi.org/10.5194/gmd-14-2867-2021, 2021.

Bao, F., Li, M., Zhang, Y., Chen, C., and Zhao, J.: Photochemical aging of Beijing urban $PM_{2.5}$: HONO production, *Environmental Science & Technology*, 52, 6309–6316, https://doi.org/10.1021/acs.est.8b00538, 2018.

Bao, Z., Zhang, X., Li, Q., Zhou, J., Shi, G., Zhou, L., Yang, F., Xie, S., Zhang, D., Zhai, C., Li, Z., Peng, C., and Chen, Y.: Measurement report: Intensive biomass burning emissions and rapid nitrate formation drive severe haze formation in the Sichuan Basin, China – insights from aerosol mass spectrometry, *Atmospheric Chemistry and Physics*, 23, 1147–1167, https://doi.org/10.5194/acp-23-1147-2023, 2023.

Barnard, J. C., Chapman, E. G., Fast, J. D., Schmelzer, J. R., Slusser, J. R., and Shetter, R. E.: An evaluation of the FAST-J photolysis algorithm for predicting nitrogen dioxide photolysis rates under clear and cloudy sky conditions, Atmos. Environ., 38, 3393–3403, https://doi.org/10.1016/j.atmosenv.2004.03.034, 2004.

Bessagnet, B., Pirovano, G., Mircea, M., Cuvelier, C., Aulinger, A., Calori, G., Ciarelli, G., Manders, A., Stern, R., Tsyro, S., García Vivanco, M., Thunis, P., Pay, M.-T., Colette, A., Couvidat, F., Meleux, F., Rouïl, L., Ung, A., Aksoyoglu, S., Baldasano, J. M., Bieser, J., Briganti, G., Cappelletti, A., D'Isidoro, M., Finardi, S., Kranenburg, R., Silibello, C., Carnevale, C., Aas, W., Dupont, J.-C., Fagerli, H., Gonzalez, L., Menut, L., Prévôt, A. S. H., Roberts, P., and White, L.: Presentation of the EURODELTA III intercomparison exercise – evaluation of the chemistry transport models' performance on criteria pollutants and joint analysis with meteorology, Atmospheric Chem. Phys., 16, 12667–12701, https://doi.org/10.5194/acp-16-12667-2016, 2016.Binkowski, F.S., Arunachalam, S., Adelman, Z., & Pinto, J. Examining photolysis rates with a prototype on-line photolysis module in CMAQ. J. Appl. Meteor. and Clim., 46, 1252-1256. doi:10.1175/JAM2531.1, 2007.

Byun, D. and Schere, K. L.: Review of the Governing Equations, Computational Algorithms, and Other Components of the Models-3 Community Multiscale Air Quality (CMAQ) Modeling System, Appl. Mech. Rev., 59, 51–77, https://doi.org/10.1115/1.2128636, 2006.

Carmichael, G. R., Sakurai, T., Streets, D., Hozumi, Y., Ueda, H., Park, S. U., Fung, C., Han, Z., Kajino, M., Engardt, M., Bennet, C., Hayami, H., Sartelet, K., Holloway, T., Wang, Z., Kannari, A., Fu, J., Matsuda, K., Thongboonchoo, N., and Amann, M.: MICS-Asia II: The model intercomparison study for Asia Phase II methodology and overview of findings, Atmos. Environ., 42, 3468–3490, https://doi.org/10.1016/j.atmosenv.2007.04.007, 2008.

Chen, L., Gao, Y., Zhang, M., Fu, J. S., Zhu, J., Liao, H., Li, J., Huang, K., Ge, B., Wang, X., Lam, Y. F., Lin, C.-Y., Itahashi, S., Nagashima, T., Kajino, M., Yamaji, K., Wang, Z., and Kurokawa, J.: MICS-Asia III: multi-model comparison and evaluation of aerosol over East Asia, Atmospheric Chem. Phys., 19, 11911–11937, https://doi.org/10.5194/acp-19-11911-2019, 2019.

CNEMC (China National Environmental Monitoring Centre): Technical Regulation for the Assessment of Urban Ambient Air Quality Index (AQI) Forecasts (Trial), Beijing, China, 2021. Available at:

https://www.cnemc.cn/zzjj/jgsz/ybzx/gzdt_ybzx/202112/t20211203_962949.shtml (last access: 8 August 2026).
Colella, P. and Woodward, P. R.: The Piecewise Parabolic Method (PPM) for gas-dynamical simulations, J. Comput. Phys., 54, 174–201, https://doi.org/10.1016/0021-9991(84)90143-8, 1984.
Crippa, M., Solazzo, E., Huang, G., Guizzardi, D., Koffi, E., Muntean, M., Schieberle, C., Friedrich, R., and Janssens-Maenhout, G.: High resolution temporal profiles in the Emissions Database for Global Atmospheric Research, Sci. Data, 7, 121, https://doi.org/10.1038/s41597-020-0462-2, 2020.Eastham, S. D., Long, M. S., Keller, C. A., Lundgren, E. W., Yantosca, R. M., Zhuang, J., Li, C., Lee, C. J., Yannetti, M., Auer, B. M., Clune, T. L., Kouatchou, J., Putman, W. M., Thompson, M. A., Trayanov, A. L., Molod, A. M., Martin, R. V., and Jacob, D. J.: GEOS-Chem High Performance (GCHP v11-02c): a next-generation implementation of the GEOS-Chem chemical transport model for massively parallel applications, Geosci. Model Dev., 11, 2941–2953, https://doi.org/10.5194/gmd-11-2941-2018, 2018.
Emery, C., Jung, J., Johnson, J., Yarwood, G., Madronich, S., Grell, G., and Boyer, D.: IMPROVING CLOUD IMPACTS ON PHOTOLYSIS USING AN ON-LINE RADIATION MODEL IN CAMx, the 9th Annual CMAS Conference, Chapel Hill, NC., 2010.
Emery, C., Jung, J., Koo, B., and Yarwood, G.: Improvements to CAMx Snow Cover Treatments and Carbon Bond Chemical Mechanism for Winter Ozone, Ramboll Environ, Novato, CA, USA, 2015.Emery, C., Baker, K., Wilson, G., and Yarwood, G.: Comprehensive Air Quality Model with Extensions: Formulation and Evaluation for Ozone and Particulate Matter over the US, Atmosphere, 15, 1158, https://doi.org/10.3390/atmos15101158, 2024.
EPA:CMAQv5.3.3 User Manual, 2021.
EPICC-Model Working Group: Description and evaluation of the Emission and atmospheric Processes Integrated and Coupled Community (EPICC) Model version 1.0, Adv. Atmospheric Sci., https://doi.org/10.1007/s00376-025-4384-y, 2026.
Foley, K. M., Roselle, S. J., Appel, K. W., Bhave, P. V., Pleim, J. E., Otte, T. L., Mathur, R., Sarwar, G., Young, J. O., Gilliam, R. C., Nolte, C. G., Kelly, J. T., Gilliland, A. B., and Bash, J. O.: Incremental testing of the Community Multiscale Air Quality (CMAQ) modeling system version 4.7, Geosci. Model Dev., 3, 205–226, https://doi.org/10.5194/gmd-3-205-2010, 2010.
Fountoukis, C. and Nenes, A.: ISORROPIA II: a computationally efficient thermodynamic equilibrium model for K+–Ca2+–Mg2+–NH4+–Na+–SO42-–NO3−–Cl−–H2O aerosols., Atmospheric Chem. Phys., 7, 4639–4659, https://doi.org/10.5194/acp-7-4639-2007, 2007.
Gao, C., Zhang, X., Xiu, A., Tong, Q., Zhao, H., Zhang, S., Yang, G., Zhang, M., and Xie, S.: Intercomparison of multiple two-way coupled meteorology and air quality models (WRF v4.1.1–CMAQ v5.3.1, WRF–Chem v4.1.1, and WRF v3.7.1–CHIMERE v2020r1) in eastern China, Geosci. Model Dev., 17, 2471–2492, https://doi.org/10.5194/gmd-17-2471-2024, 2024.
Gao, M., Han, Z., Liu, Z., Li, M., Xin, J., Tao, Z., Li, J., Kang, J.-E., Huang, K., Dong, X., Zhuang, B., Li, S., Ge, B., Wu, Q., Cheng, Y., Wang, Y., Lee, H.-J., Kim, C.-H., Fu, J. S., Wang, T., Chin, M., Woo, J.-H., Zhang, Q., Wang, Z., and Carmichael, G. R.: Air quality and climate change, Topic 3 of the Model Inter-Comparison Study for Asia Phase III (MICS-Asia III) – Part 1: Overview and model evaluation, Atmospheric Chem. Phys., 18, 4859–4884, https://doi.org/10.5194/acp-18-4859-2018, 2018.
Gao, Y., Yan, F., Ma, M., Ding, A., Liao, H., Wang, S., Wang, X., Zhao, B., Cai, W., Su, H., Yao, X.,

and Gao, H.: Unveiling the dipole synergic effect of biogenic and anthropogenic emissions on ozone concentrations, Sci. Total Environ., 818, 151722, https://doi.org/10.1016/j.scitotenv.2021.151722, 2022.
Gao, Z. and Zhou, X.: A review of the CAMx, CMAQ, WRF-Chem and NAQPMS models: Application, evaluation and uncertainty factors, Environ. Pollut., 343, 123183, https://doi.org/10.1016/j.envpol.2023.123183, 2024.
Geng, G., Liu, Y., Liu, Y., Liu, S., Cheng, J., Yan, L., Wu, N., Hu, H., Tong, D., Zheng, B., Yin, Z., He, K., and Zhang, Q.: Efficacy of China's clean air actions to tackle $PM_{2.5}$ pollution between 2013 and 2020, Nat. Geosci., 17, 987–994, https://doi.org/10.1038/s41561-024-01540-z, 2024.
GEOS-Chem model description and reference guide, version 14.5.1, Zenodo, https://doi.org/10.5281/zenodo.14629792, 2025.
Gong, C. and Liao, H.: A typical weather pattern for ozone pollution events in North China, Atmospheric Chem. Phys., 19, 13725–13740, https://doi.org/10.5194/acp-19-13725-2019, 2019.Grell, G. A., Peckham, S. E., Schmitz, R., McKeen, S. A., Frost, G., Skamarock, W. C., and Eder, B.:Fully coupled "online" chemistry within the WRF model, Atmos. Environ., 39, 6957–6975, https://doi.org/10.1016/j.atmosenv.2005.04.027, 2005.
Guenther, A. B., Jiang, X., Heald, C. L., Sakulyanontvittaya, T., Duhl, T., Emmons, L. K., and Wang, X.: The Model of Emissions of Gases and Aerosols from Nature version 2.1 (MEGAN2.1): an extended and updated framework for modeling biogenic emissions, Geosci. Model Dev., 5, 1471–1492, https://doi.org/10.5194/gmd-5-1471-2012, 2012.
Haagen-Smit, A. J. and Fox, M. M.: Ozone formation in photochemical oxidation of organic substances, *Industrial & Engineering Chemistry*, 48, 1484–1487, https://doi.org/10.1021/ie51400a033, 1956.
Hong, C., Zhang, Q., He, K., Guan, D., Li, M., Liu, F., and Zheng, B.: Variations of China's emission estimates: response to uncertainties in energy statistics, Atmospheric Chem. Phys., 17, 1227–1239, https://doi.org/10.5194/acp-17-1227-2017, 2017.
Hong, S.-Y., Noh, Y., and Dudhia, J.: A New Vertical Diffusion Package with an Explicit Treatment of Entrainment Processes, Mon. Weather Rev., 134, 2318–2341, https://doi.org/10.1175/MWR3199.1, 2006.
Huang, L., Zhu, Y., Zhai, H., Xue, S., Zhu, T., Shao, Y., Liu, Z., Emery, C., Yarwood, G., Wang, Y., Fu, J., Zhang, K., and Li, L.: Recommendations on benchmarks for numerical air quality model applications in China – Part 1: $PM_{2.5}$ and chemical species, Atmospheric Chem. Phys., 21, 2725–2743, https://doi.org/10.5194/acp-21-2725-2021, 2021.
Huang, L., Liu, H., Yarwood, G., Wilson, G., Tao, J., Han, Z., Ji, D., Wang, Y., and Li, L.: Modeling of secondary organic aerosols (SOA) based on two commonly used air quality models in China: Consistent S/IVOCs contribution but large differences in SOA aging, Sci. Total Environ., 903, 166162, https://doi.org/10.1016/j.scitotenv.2023.166162, 2023.
Huang, X., Song, Y., Li, M., Li, J., Huo, Q., Cai, X., Zhu, T., Hu, M., and Zhang, H.: A high-resolution ammonia emission inventory in China, Glob. Biogeochem. Cycles, 26, https://doi.org/10.1029/2011GB004161, 2012a.
Huang, X., Li, M., Li, J., and Song, Y.: A high-resolution emission inventory of crop burning in fields in China based on MODIS Thermal Anomalies/Fire products, Atmos. Environ., 50, 9–15, https://doi.org/10.1016/j.atmosenv.2012.01.017, 2012b.
Iacono, M. J., Delamere, J. S., Mlawer, E. J., Shephard, M. W., Clough, S. A., and Collins, W. D.:

Radiative forcing by long-lived greenhouse gases: Calculations with the AER radiative transfer models, J. Geophys. Res. Atmospheres, 113, https://doi.org/10.1029/2008JD009944, 2008.

Itahashi, S., Ge, B., Sato, K., Fu, J. S., Wang, X., Yamaji, K., Nagashima, T., Li, J., Kajino, M., Liao, H., Zhang, M., Wang, Z., Li, M., Kurokawa, J., Carmichael, G. R., and Wang, Z.: MICS-Asia III: overview of model intercomparison and evaluation of acid deposition over Asia, Atmospheric Chem. Phys., 20, 2667–2693, https://doi.org/10.5194/acp-20-2667-2020, 2020.

Jia, W., Zhang, X., Wang, H., Wang, Y., Wang, D., Zhong, J., Zhang, W., Zhang, L., Guo, L., Lei, Y., Wang, J., Yang, Y., and Lin, Y.: Comprehensive evaluation of typical planetary boundary layer (PBL) parameterization schemes in China – Part 1: Understanding expressiveness of schemes for different regions from the mechanism perspective, Geosci. Model Dev., 16, 6635–6670, https://doi.org/10.5194/gmd-16-6635-2023, 2023.

Jiang, F., Guo, H., Wang, T. J., Cheng, H. R., Wang, X. M., Simpson, I. J., Ding, A. J., Saunders, S. M., Lam, S. H. M., and Blake, D. R.: An ozone episode in the Pearl River Delta: Field observation and model simulation, J. Geophys. Res. Atmospheres, 115, 2009JD013583, https://doi.org/10.1029/2009JD013583, 2010.

Jiménez, P. A. and Dudhia, J.: On the Ability of the WRF Model to Reproduce the Surface Wind Direction over Complex Terrain, J. Appl. Meteorol. Climatol., 52, 1610–1617, https://doi.org/10.1175/JAMC-D-12-0266.1, 2013.

Jing, Z., Liu, P., Wang, T., Song, H., Lee, J., Xu, T., and Xing, Y.: Effects of Meteorological Factors and Anthropogenic Precursors on PM2.5 Concentrations in Cities in China, Sustainability, 12, 3550, https://doi.org/10.3390/su12093550, 2020.

Kain, J. S.: The Kain–Fritsch Convective Parameterization: An Update, J. Appl. Meteorol., 43, 170–181, https://doi.org/10.1175/1520-0450(2004)043%253C0170:TKCPAU%253E2.0.CO;2, 2004.

Kang, Y., Liu, M., Song, Y., Huang, X., Yao, H., Cai, X., Zhang, H., Kang, L., Liu, X., Yan, X., He, H., Zhang, Q., Shao, M., and Zhu, T.: High-resolution ammonia emissions inventories in China from 1980 to 2012, Atmospheric Chem. Phys., 16, 2043–2058, https://doi.org/10.5194/acp-16-2043-2016, 2016.Kim, D.-J., Kim, T.-H., Choi, J.-Y., Lee, J., Kim, R.-H., Son, J.-S., and Lee, D.: The Impact of Vertical Eddy Diffusivity Changes in the CMAQ Model on PM2.5 Concentration Variations in Northeast Asia: Focusing on the Seoul Metropolitan Area, Atmosphere, 15, 376, https://doi.org/10.3390/atmos15030376, 2024.

Kong, L., Tang, X., Zhu, J., Wang, Z., Pan, Y., Wu, H., Wu, L., Wu, Q., He, Y., Tian, S., Xie, Y., Liu, Z., Sui, W., Han, L., and Carmichael, G.: Improved Inversion of Monthly Ammonia Emissions in China Based on the Chinese Ammonia Monitoring Network and Ensemble Kalman Filter, Environ. Sci. Technol., 53, 12529–12538, https://doi.org/10.1021/acs.est.9b02701, 2019.

Li, B., Gao, J., Chen, C., Wen, L., Zhang, Y., Li, J., Zhang, Y., Du, X., Zhang, K., and Wang, J.: Exploring HONO production from particulate nitrate photolysis in representative regions of China: characteristics, influencing factors, and environmental implications, *Atmospheric Chemistry and Physics*, 24, 13183–13198, https://doi.org/10.5194/acp-24-13183-2024, 2024.

Li, J., Nagashima, T., Kong, L., Ge, B., Yamaji, K., Fu, J. S., Wang, X., Fan, Q., Itahashi, S., Lee, H.-J., Kim, C.-H., Lin, C.-Y., Zhang, M., Tao, Z., Kajino, M., Liao, H., Li, M., Woo, J.-H., Kurokawa, J., Wang, Z., Wu, Q., Akimoto, H., Carmichael, G. R., and Wang, Z.: Model evaluation and intercomparison of surface-level ozone and relevant species in East Asia in the context of MICS-Asia Phase III – Part 1: Overview, Atmospheric Chem. Phys., 19, 12993–

13015, https://doi.org/10.5194/acp-19-12993-2019, 2019a.
Li, K., Jacob, D. J., Liao, H., Zhu, J., Shah, V., Shen, L., Bates, K. H., Zhang, Q., and Zhai, S.: A two-pollutant strategy for improving ozone and particulate air quality in China, Nat. Geosci., 12, 906–910, https://doi.org/10.1038/s41561-019-0464-x, 2019b.
Li, R., Ma, X., Xiong, F., Jia, H., Sha, T., and Tian, R.: Comparisons and evaluation of aerosol burden and optical depth in CMIP5 simulations over East Asia, J. Atmospheric Sol.-Terr. Phys., 206, 105315, https://doi.org/10.1016/j.jastp.2020.105315, 2020.
Li, X., Hussain, S. A., Sobri, S., and Md Said, M. S.: Overviewing the air quality models on air pollution in Sichuan Basin, China, Chemosphere, 271, 129502, https://doi.org/10.1016/j.chemosphere.2020.129502, 2021.
Li, X., Che, H., Wang, H., Xia, X., Chen, Q., Gui, K., Zhao, H., An, L., Zheng, Y., Sun, T., Sheng, Z., Liu, C., and Zhang, X.: Spatial and temporal distribution of the cloud optical depth over China based on MODIS satellite data during 2003–2016, J. Environ. Sci., 80, 66–81, https://doi.org/10.1016/j.jes.2018.08.010, 2019.
Liu, Z., Zhou, M., Chen, Y., Chen, D., Pan, Y., Song, T., Ji, D., Chen, Q., and Zhang, L.: The nonlinear response of fine particulate matter pollution to ammonia emission reductions in North China, Environ. Res. Lett., https://doi.org/10.1088/1748-9326/abdf86, 2021.
Lou, M., Wu, Q., Li, J., Cheng, H., Zhu, J., Wang, L., and Wang, Z.: The amplification effect of El Niño on winter heavy pollution frequency in Beijing, Environ. Res. Lett., 20, 074043, https://doi.org/10.1088/1748-9326/ade1ee, 2025.
Lyu, Y., Wu, D., Han, F., Zhang, H., Lv, F., Kang, A., Hu, Y., and Pang, X.: Co-Occurring Extremes of $PM_{2.5}$ and Ozone in Warm Seasons of the Yangtze River Delta of China: Insights from Explainable Machine Learning, ACS EST Air, 2, 578–588, https://doi.org/10.1021/acsestair.4c00314, 2025.MEE (Ministry of Ecology and Environment of the People's Republic of China): Technical Guideline for Numerical Forecasting of Ambient Air Quality (HJ 1130–2020), Beijing, China, 2020. Available at: https://www.mee.gov.cn/ywgz/fgbz/bz/bzwb/jcffbz/202005/t20200518_779714.shtml (last access: 8 August 2026).
Miao, R., Chen, Q., Zheng, Y., Cheng, X., Sun, Y., Palmer, P. I., Shrivastava, M., Guo, J., Zhang, Q., Liu, Y., Tan, Z., Ma, X., Chen, S., Zeng, L., Lu, K., and Zhang, Y.: Model bias in simulating major chemical components of $PM_{2.5}$ in China, Atmospheric Chem. Phys., 20, 12265–12284, https://doi.org/10.5194/acp-20-12265-2020, 2020.
Murphy, B. N., Woody, M. C., Jimenez, J. L., Carlton, A. M. G., Hayes, P. L., Liu, S., Ng, N. L., Russell, L. M., Setyan, A., Xu, L., Young, J., Zaveri, R. A., Zhang, Q., and Pye, H. O. T.: Semivolatile POA and parameterized total combustion SOA in CMAQv5.2: impacts on source strength and partitioning, Atmospheric Chem. Phys., 17, 11107–11133, https://doi.org/10.5194/acp-17-11107-2017, 2017.
NASA: Tropospheric ultraviolet and visible (TUV) radiation model. https://www2.acom.ucar.edu/modeling/tropospheric-ultraviolet-and-visible-tuv-radiation-model (2024), Accessed 12th Feb 2026.
NCEP: NCEP FNL Operational Model Global Tropospheric Analyses, continuing from July 1999, National Centers for Environmental Prediction [data set], https://doi.org/10.5065/D6M043C6, 2000.
Nenes, A., Pandis, S. N., and Pilinis, C.: ISORROPIA: A New Thermodynamic Equilibrium Model

for Multiphase Multicomponent Inorganic Aerosols, Aquat. Geochem., 4, 123–152, https://doi.org/10.1023/A:1009604003981, 1998.
Odum, J. R., W, J. T. P., C, F. R., and H, S. J.: The Atmospheric Aerosol-Forming Potential of Whole Gasoline Vapor., Science, 276, 96–99, 1997.
Oyegbile, O., Chan, A., Ooi, M., Anwar, P., Mohamed, A. A., and Li, L.: Evaluation of WRF model performance with different microphysics schemes for extreme rainfall prediction in Lagos, Nigeria: Implications for urban flood risk management, Bull. Atmospheric Sci. Technol., 5, 19, https://doi.org/10.1007/s42865-024-00081-y, 2024.
Pandis, S. N., Harley, R. A., Cass, G. R., and Seinfeld, J. H.: Secondary organic aerosol formation and transport, Atmos. Environ., 26, 2269–2282, https://doi.org/10.1016/0960-1686(92)90358-r, 1992.
Pennington, E. A., Seltzer, K. M., Murphy, B. N., Qin, M., Seinfeld, J. H., and Pye, H. O. T.: Modeling secondary organic aerosol formation from volatile chemical products, Atmospheric Chem. Phys., 21, 18247–18261, https://doi.org/10.5194/acp-21-18247-2021, 2021.
Pleim, J. E.: A Combined Local and Nonlocal Closure Model for the Atmospheric Boundary Layer. Part I: Model Description and Testing, J. Appl. Meteorol. Climatol., 46, 1383–1395, https://doi.org/10.1175/JAM2539.1, 2007.
Ramboll: CAMx User's Guide v7.00, 2020.
Ren, F., Lin, J., Xu, C., Adeniran, J. A., Wang, J., Martin, R. V., van Donkelaar, A., Hammer, M. S., Horowitz, L. W., Turnock, S. T., Oshima, N., Zhang, J., Bauer, S., Tsigaridis, K., Seland, Ø., Nabat, P., Neubauer, D., Strand, G., van Noije, T., Le Sager, P., and Takemura, T.: Evaluation of CMIP6 model simulations of $PM_{2.5}$ and its components over China, Geosci. Model Dev., 17, 4821–4836, https://doi.org/10.5194/gmd-17-4821-2024, 2024.
Ren, J., Guo, F., and Xie, S.: Diagnosing ozone–NO_x–VOC sensitivity and revealing causes of ozone increases in China based on 2013–2021 satellite retrievals, Atmospheric Chem. Phys., 22, 15035–15047, https://doi.org/10.5194/acp-22-15035-2022, 2022.
Powers, J. G., Klemp, J. B., Skamarock, W. C., Davis, C. A., Dudhia, J., Gill, D. O., Coen, J. L., Gochis, D. J., Ahmadov, R., Peckham, S. E., Grell, G. A., Michalakes, J., Trahan, S., Benjamin, S. G., Alexander, C. R., Dimego, G. J., Wang, W., Schwartz, C. S., Liu, Z., Snyder, C., Chen, F., Barlage, M., Yu, W., and Duda, M. G.: The Weather Research and Forecasting Model: Overview, system efforts, and future directions, Bull. Am. Meteorol. Soc., 98, 1717–1737, https://doi.org/10.1175/BAMS-D-15-00308.1, 2017.
Seinfeld, J. H. and Pandis, S. N.: Atmospheric Chemistry and Physics: From Air Pollution to Climate Change, 3rd Edition, Wiley, 2016.
Shao, J., Chen, Q., Wang, Y., Lu, X., He, P., Sun, Y., Shah, V., Martin, R. V., Philip, S., Song, S., Zhao, Y., Xie, Z., Zhang, L., and Alexander, B.: Heterogeneous sulfate aerosol formation mechanisms during wintertime Chinese haze events: air quality model assessment using observations of sulfate oxygen isotopes in Beijing, Atmospheric Chem. Phys., 19, 6107–6123, https://doi.org/10.5194/acp-19-6107-2019, 2019.
Sillman, S.: The relation between ozone, NOx and hydrocarbons in urban and polluted rural environments, Atmos. Environ., 33, 1821–1845, https://doi.org/10.1016/S1352-2310(98)00345-8, 1999.
Skamarock, W. C., Klemp, J. B., Dudhia, J., Gill, D. O., Barker, D., Duda, M. G., Huang, X. Y., Wang W., and Powers, J. G.: A description of the Advanced Research WRF version 3, NCAR

Technical note-475+ STR, https://doi.org/10.5065/D68S4MVH, 2008.
Song, Y., Liu, B., Miao, W., Chang, D., and Zhang, Y.: Spatiotemporal variation in nonagricultural open fire emissions in China from 2000 to 2007, Glob. Biogeochem. Cycles, 23, 2008GB003344, https://doi.org/10.1029/2008GB003344, 2009.
Tang, W., Cohan, D. S., Morris, G. A., Byun, D. W., and Luke, W. T.: Influence of vertical mixing uncertainties on ozone simulation in CMAQ, Atmos. Environ., 45, 2898–2909, https://doi.org/10.1016/j.atmosenv.2011.01.057, 2011.
Tewari, M., Chen, F., Wang, W., Dudhia, J., LeMone, M. A., Gayno, G., Wegiel, J., and Cuenca, R. H.: A IMPLEMENTATION AND VERIFICATION OF THE UNIFIED NOAH LAND SURFACE MODEL IN THE WRF MODEL, 20th Conf. Weather Anal. Forecast. Conf. Numer. Weather Predict., 11–15, 2004.
Thompson, G., Field, P. R., Rasmussen, R. M., and Hall, W. D.: Explicit Forecasts of Winter Precipitation Using an Improved Bulk Microphysics Scheme. Part II: Implementation of a New Snow Parameterization, Mon. Weather Rev., 136, 5095–5115, https://doi.org/10.1175/2008MWR2387.1, 2008.
US EPA: CMAQ, , https://doi.org/10.5281/zenodo.5213949, 2021.
Walcek, C. J. and Aleksic, N. M.: A simple but accurate mass conservative, peak-preserving, mixing ratio bounded advection algorithm with FORTRAN code, Atmos. Environ., 32, 3863–3880, https://doi.org/10.1016/S1352-2310(98)00099-5, 1998.
Walcek, C. J. and Taylor, G. R.: A Theoretical Method for Computing Vertical Distributions of Acidity and Sulfate Production within Cumulus Clouds, J. Atmospheric Sci., 43, 339–355, 1986.
Wang, H., Lu, X., Palmer, P. I., Zhang, L., Lu, K., Li, K., Nagashima, T., Koo, J.-H., Tanimoto, H., Wang, H., Gao, M., He, C., Wu, K., Fan, S., and Zhang, Y.: Deciphering decadal urban ozone trends from historical records since 1980, Natl. Sci. Rev., 11, nwae369, https://doi.org/10.1093/nsr/nwae369, 2024.
Wang, W., Li, X., Shao, M., Hu, M., Zeng, L., Wu, Y., and Tan, T.: The impact of aerosols on photolysis frequencies and ozone production in Beijing during the 4-year period 2012–2015, Atmospheric Chem. Phys., 19, 9413–9429, https://doi.org/10.5194/acp-19-9413-2019, 2019.
Wang, W., Liu, M., Wang, T., Song, Y., Zhou, L., Cao, J., Hu, J., Tang, G., Chen, Z., Li, Z., Xu, Z., Peng, C., Lian, C., Chen, Y., Pan, Y., Zhang, Y., Sun, Y., Li, W., Zhu, T., Tian, H., and Ge, M.: Sulfate formation is dominated by manganese-catalyzed oxidation of SO2 on aerosol surfaces during haze events, Nat. Commun., 12, 1993, https://doi.org/10.1038/s41467-021-22091-6, 2021.
Wang, W., Chen, H., Wang, Z., Li, J., Chen, X., Yu, F., Fan, X., Zhao, S., Hu, B., Wang, W., Tang, X., Wang, Z., Ge, B., and Wu, J.: Development and evaluation of photolysis and gas-phase reaction scheme in EPICC-model: Impacts on tropospheric ozone simulation, Atmos. Environ., 359, 121373, https://doi.org/10.1016/j.atmosenv.2025.121373, 2025.
Wang, X., Zhang, Y., Hu, Y., Zhou, W., Lu, K., Zhong, L., Zeng, L., Shao, M., Hu, M., and Russell, A. G.: Process analysis and sensitivity study of regional ozone formation over the Pearl River Delta, China, during the PRIDE-PRD2004 campaign using the Community Multiscale Air Quality modeling system, Atmospheric Chem. Phys., 10, 4423–4437, https://doi.org/10.5194/acp-10-4423-2010, 2010.
Wang, Y., Jiang, S., Huang, L., Lu, G., Kasemsan, M., Yaluk, E. A., Liu, H., Liao, J., Bian, J., Zhang,

K., Chen, H., and Li, L.: Differences between VOCs and NOx transport contributions, their impacts on O3, and implications for O3 pollution mitigation based on CMAQ simulation over the Yangtze River Delta, China, Sci. Total Environ., 872, 162118, https://doi.org/10.1016/j.scitotenv.2023.162118, 2023.

Wen, W.; Shen, S.; Liu, L.; Ma, X.; Wei, Y.; Wang, J.; Xing, Y.; Su, W. Comparative Analysis of $PM_{2.5}$ and O_3 Source in Beijing Using a Chemical Transport Model. *Remote Sens.* 2021, *13*, 3457. https://doi.org/10.3390/rs13173457.

William, H.: III. Experiments on the quantity of gases absorbed by water, at different temperatures, and under different pressures, Philos. Trans. R. Soc. Lond., https://doi.org/10.1098/rstl.1803.0004, 1803.

Wu, Q., Wang, Z., Chen, H., Zhou, W., and Wenig, M.: An evaluation of air quality modeling over the Pearl River Delta during November 2006, Meteorol. Atmospheric Phys., 116, 113–132, https://doi.org/10.1007/s00703-011-0179-z, 2012.

Xiao, Q., Geng, G., Xue, T., Liu, S., Cai, C., He, K., and Zhang, Q.: Tracking $PM_{2.5}$ and O3 Pollution and the Related Health Burden in China 2013–2020, Environ. Sci. Technol., 56, 6922–6932, https://doi.org/10.1021/acs.est.1c04548, 2022.

Xu, W., Ning, L., and Luo, Y.: Applying Satellite Data Assimilation to Wind Simulation of Coastal Wind Farms in Guangdong, China, Remote Sens., 12, 973, https://doi.org/10.3390/rs12060973, 2020.

Yang, J., Qu, Y., Chen, Y., Zhang, J., Liu, X., Niu, H., and An, J.: Dominant physical and chemical processes impacting nitrate in Shandong of the North China Plain during winter haze events, Sci. Total Environ., 912, 169065, https://doi.org/10.1016/j.scitotenv.2023.169065, 2024.

Yarwood, G., Yocke, S. R. M., and Whitten, G.: Updates to the Carbon Bond Mechanism: CB05, U.S. Environmental Protection Agency, 2005.

Yarwood, G., Beardsley, R., and Shi, Y.: Revision 5 of the Carbon Bond 6 Mechanism (CB6r5), 2020.

Yu, E., Ma, J., and Sun, J.: Developing a Climate Prediction System over Southwest China Using the 8-km Weather Research and Forecasting (WRF) Model: System Design, Model Calibration, and Performance Evaluation, Weather Forecast., 37, 1703–1719, https://doi.org/10.1175/WAF-D-21-0188.1, 2022a.

Yu, E., Bai, R., Chen, X., and Shao, L.: Impact of physical parameterizations on wind simulation with WRF V3.9.1.1 under stable conditions at planetary boundary layer gray-zone resolution: a case study over the coastal regions of North China, Geosci. Model Dev., 15, 8111–8134, https://doi.org/10.5194/gmd-15-8111-2022, 2022b.

Zhai, S., Jacob, D. J., Wang, X., Liu, Z., Wen, T., Shah, V., Li, K., Moch, J. M., Bates, K. H., Song, S., Shen, L., Zhang, Y., Luo, G., Yu, F., Sun, Y., Wang, L., Qi, M., Tao, J., Gui, K., Xu, H., Zhang, Q., Zhao, T., Wang, Y., Lee, H. C., Choi, H., and Liao, H.: Control of particulate nitrate air pollution in China, Nature Geoscience, 14, 389-395, https://doi.org/10.1038/s41561-021-00726-z, 2021.

Zhang, J., Lian, C., Wang, W., Ge, M., Guo, Y., Ran, H., Zhang, Y., Zheng, F., Fan, X., Yan, C., Daellenbach, K. R., Liu, Y., Kulmala, M., and An, J.: Amplified role of potential HONO sources in O_3 formation in North China Plain during autumn haze aggravating processes, Atmospheric Chem. Phys., 22, 3275–3302, https://doi.org/10.5194/acp-22-3275-2022, 2022.

Zhang, J. L., Wang, W. D., Zhu, K. Y., Huang, Z. J., Sheng, L., Liao, S. D., Yuan, X., Hu, Y. N.,

Liu, J. P., Tang, M. X., Huang, X. F., Li, J., Wang, Z. F., and Zheng, J. Y.: The potentials of uncertainty analysis and Bayesian optimization in HONO source modeling diagnosis and improvement, *Environmental Research*, 276, 121494, https://doi.org/10.1016/j.envres.2025.121494, 2025.

Zhang, L., Gong, S., Padro, J., and Barrie, L.: A size-segregated particle dry deposition scheme for an atmospheric aerosol module, Atmos. Environ., 35, 549–560, https://doi.org/10.1016/S1352-2310(00)00326-5, 2001.

Zhang, L., Brook, J. R., and Vet, R.: A revised parameterization for gaseous dry deposition in air-quality models, Atmospheric Chem. Phys., 3, 2067–2082, https://doi.org/10.5194/acp-3-2067-2003, 2003.

Zhang, X. Y., Wang, Y. Q., Niu, T., Zhang, X. C., Gong, S. L., Zhang, Y. M., and Sun, J. Y.: Atmospheric aerosol compositions in China: spatial/temporal variability, chemical signature, regional haze distribution and comparisons with global aerosols, Atmospheric Chem. Phys., 12, 779–799, https://doi.org/10.5194/acp-12-779-2012, 2012.

Zhu, Q., Yu, Y., Gong, H., Wang, Y., Wang, H., Wang, W., Xu, B., and Cheng, T.: Spatio-temporal characteristics of $PM_{2.5}$ and O3 synergic pollutions and influence factors in the Yangtze River Delta, Front. Environ. Sci., https://doi.org/10.3389/fenvs.2022.1104013, 2023.